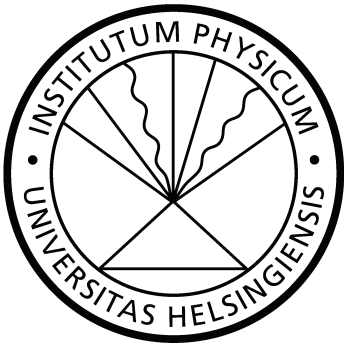

Master's Thesis
Theoretical Physics

Detection of soil permittivity and soil freezing using satellite microwave radars

Tuomo Smolander
March 2018

Supervisors: Juha Lemmetyinen, Finnish Meteorological Institute
Kimmo Rautiainen, Finnish Meteorological Institute
Examiners: Matti Leppäranta, University of Helsinki
Kari Rummukainen, University of Helsinki

UNIVERSITY OF HELSINKI
DEPARTMENT OF PHYSICS

P.O.Box 64 (Gustaf Hällströmin katu 2)
FI-00014 University of Helsinki

HELSINGIN YLIOPISTO — HELSINGFORS UNIVERSITET — UNIVERSITY OF HELSINKI

Tiedekunta/Osasto — Fakultet/Sektion — Faculty	Laitos — Institution — Department
Faculty of Science	Department of Physics

Tekijä — Författare — Author
Tuomo Smolander

Työn nimi — Arbetets titel — Title

Detection of soil permittivity and soil freezing using satellite microwave radars

Oppiaine — Läroämne — Subject
Theoretical physics

Työn laji — Arbetets art — Level	Aika — Datum — Month and year	Sivumäärä — Sidoantal — Number of pages
Master's thesis	March 2018	63 pages

Tiivistelmä — Referat — Abstract

Remote sensing of soil permittivity and soil freezing was investigated using two different satellite based microwave radars: ASCAT and ASAR. ASCAT is a scatterometer with a good temporal resolution but coarse spatial resolution. ASAR is a synthetic aperture radar and has fine spatial resolution, but lacks good temporal coverage.

Soil permittivity is related to soil moisture, which is considered an essential climate variable since it has an effect on both weather and climate. Soil freezing affects hydrological and carbon cycles, surface energy balance, photosynthesis of vegetation and the activity of soil microbes.

A semi-empirical model for backscattering of forested land was used to acquire soil permittivity retrievals from satellite measurements using the method of least squares. The onset of soil freezing was determined from the permittivity retrievals using a simple threshold method.

A five year time series of satellite observations from July 2007 to June 2012 (April 2012 for ASAR) was investigated in Sodankylä in Northern Finland. The satellite based retrievals were compared against *in situ* measurements of soil permittivity, soil temperature, soil frost and snow depth.

According to the results the satellite permittivity retrievals correlate with each other, but not with *in situ* permittivity measurements. ASCAT retrieval shows some correlation with *in situ* temperature measurements, which could impair its correlation with *in situ* permittivity. The explanation for this phenomenon needs further research.

Comparison of soil freezing onset dates from satellite retrievals with *in situ* soil temperature and soil frost measurements showed quite good agreement for most years, and did not seem to be affected by first snowfall, even though the permittivity retrievals appeared to react in a similar way to snow cover and soil freezing. This indicates that with better calibration of the permittivity threshold limit this method could be used for soil freeze detection. Auxiliary information about air temperature and snow cover could also be used to filter out possible false estimates before freezing and after the snow cover starts to affect the satellite retrievals.

Avainsanat — Nyckelord — Keywords
Remote sensing, microwave radar, backscattering model, soil permittivity, soil freezing

Säilytyspaikka — Förvaringsställe — Where deposited

Muita tietoja — övriga uppgifter — Additional information

Pakkanen puhurin poika,
älä kylmä kynsiäni,
älä päätäni palella,
kylmä soita, kylmä maita,
kylmä kovia kallioita!

TRAD.

Acknowledgements

First and foremost, I want to thank Finnish Meteorological Institute and especially Jouni Pulliainen and Juha Lemmetyinen for providing the topic for this work, as well as resources and a workplace to execute it. Juha has also acted as a supervisor for this work together with Kimmo Rautiainen, for which I'm very grateful to both of them. I would also like to thank Vienna University of Technology and Gamma Remote Sensing for providing the satellite data used in this work, as well as my colleague Juval Cohen for preparing auxiliary datasets for me.

Several people at *!reson* IRC-channel have answered many questions regarding practicalities associated with this work, which has been very helpful, and for which I'm grateful to them. My father Heikki Smolander also deserves many thanks for providing additional assistance and consultation for this work.

I also want to thank prof. Matti Leppäranta for examining this work on the verge of retirement as well as prof. Kari Rummukainen for acting as a second examiner and also for providing guidance regarding this work and my studies at the University of Helsinki.

Contents

List of acronyms

AIEM	Advanced Integral Equation Model
ASCAT	Advanced Scatterometer
ASAR	Advanced Synthetic Aperture Radar
C-band	frequency band 4–18 GHz
CCI	Climate Change Initiative
Envisat	Environmental Satellite
ESA	European Space Agency
Eumetsat	European Organisation for the Exploitation of Meteorological Satellites
FMI	Finnish Meteorological Institute
HH	horizontal-horizontal like-polarization
HV	horizontal-vertical cross-polarization
IEM	Integral Equation Model
ISMN	International Soil Moisture Network
LAI	Leaf Area Index
MetOp	Meteorological Operational
MIMICS	Michigan Microwave Canopy Scattering Model
NASA	National Aeronautics and Space Administration
NDVI	Normalized Difference Vegetation Index
RMSE	Root Mean Square Error
SAR	Synthetic Aperture Radar
SMAP	Soil Moisture Active Passive
SMOS	Soil Moisture and Ocean Salinity
STD	standard deviation
SYKE	Finnish Environment Institute
UV	ultraviolet
VH	vertical-horizontal cross-polarization
VV	vertical-vertical like-polarization

Chapter 1

Introduction

1.1 Remote sensing using active microwave sensors

This work deals with remote sensing using space borne active microwave sensors. Remote sensing means gathering of information at a distance. [1] The specific field of remote sensing this work falls into is about observing Earth's surface using air or space borne instruments measuring electromagnetic energy. These instruments can be divided into two categories: active and passive instruments. Active instruments use their own energy to illuminate the target and to measure the reflected energy. Passive instruments measure energy originating from some other source (in practice the Sun) which is either reflected or absorbed and emitted by the target.

Electromagnetic spectrum covers a wide range of wavelengths. From shortest wavelength to longest the spectrum is divided into gamma rays, X-rays, ultraviolet, visible light, infrared, microwaves and radio waves. Several of these can be used for remote sensing. Microwaves, which are used in this work, have a wavelength between about one millimeter to about one meter and can be used to make observations in almost any cloud and weather conditions. Shorter wavelength improves spatial resolution, longer wavelength has better penetration for example into the soil. [1] Microwaves are further divided into different bands which are named using varying letters. Instruments in this work fall into the C-band, which covers frequencies 4–18 GHz and wavelengths 3.75–7.5 cm.

Active microwave instruments are radars (an acronym for "radio detection and ranging"). They transmit a microwave signal and then measure the scattered wave in the direction of the receiver. The elementary parts of radar system are a transmitter, a receiver, an antenna, and a recorder. A transmitter transmits microwave energy at a specific frequency and sends it to antenna. A receiver receives reflected signal from antenna. An antenna is needed both for transmitting and receiving the signal and usually the same antenna is used for both functions. A recorder is used for recording and displaying the received signal. Radars can be used from aircraft ("air borne"), satellites ("space borne") or ground based towers.

Scatterometers are pulse radars that send short electromagnetic pulses and measure the power of the backscattered signal from the target. They are real aperture radars which means that the beamwidth is controlled by the physical antenna length. For this reason their maximum spatial resolution is often quite limited. Their advantages are simple design and data processing and good temporal resolution. [2]

Synthetic Aperture Radars (SAR) are also active instruments like scatterometers. In synthetic aperture radars the movement of the instrument is used to simulate a greater antenna length than what the antenna actually has. [2] This enables much better spatial resolution than with real aperture radars. The downside is that the spatial and temporal coverage are much lower.

1.2 Applications of radar measurements in remote sensing

1.2.1 Soil moisture and permittivity

Soil moisture is considered an essential climate variable because it affects both weather and climate. It is important for understanding land surface processes since soil moisture affects hydrological processes, carbon cycle, and energy exchange between soil, vegetation, and atmosphere. Climate models, hydrological models, and numerical weather prediction models use soil moisture as a variable. It is also related to soil engineering questions and can be used for monitoring the effects of climate change.

The traditional method for measuring soil moisture is to carry out *in situ* mea-

surements. These give good information about the local situation, but are inapplicable at larger spatial scales. Satellite remote sensing enables continuous global scale observations.

Automatic *in situ* measurements are based on measuring the dielectricity of soil. The same principle applies when estimating soil moisture using microwave instruments because changes in permittivity also affect backscattering, and permittivity is heavily influenced by moisture. [1] Dielectric permittivity can be converted to soil moisture using a model presented by Dobson et al. [3], which is applicable for varying soil compositions, or using relations by Topp et al. [4] for mineral soils, and Bircher et al. [5] for organic soils. [6] Models can be calibrated by gathering samples from terrain and measuring their water content in a laboratory.

Soil moisture has been interpreted from satellite measurements even when that has not been the specific purpose of the satellite mission. [7] There have also been missions with specific focus on soil moisture. European Space Agency's (ESA) Soil Moisture and Ocean Salinity (SMOS) mission has been designed to observe soil moisture over land and salinity over the oceans using passive microwave radiometer measurements. It was launched in 2009. [8] National Aeronautics and Space Administration's (NASA) Soil Moisture Active Passive (SMAP) mission has been designed to measure the moisture of topmost soil layer around the globe and also to detect if the ground is frozen or thawed, and it incorporates both an active radar and a passive radiometer within same mission. It was launched in January 2015, but the active instrument ceased to work in July 2015. [9]

Existing products

The International Soil Moisture Network (ISMN) is a database that combines several *in situ* measurement networks around the globe into one place for validating satellite observations and land surface models and also to help to improve them. It contains over 2400 stations from 59 networks. [10] Unfortunately these stations are not located homogeneously around the world, but are concentrated in northern hemisphere, especially in the USA and Europe. This combined with the fact that *in situ* measurements are at point scale whereas remote sensing pixels can be at kilometer scale, make soil moisture measuring and verification at global scale challenging.

European Space Agency's Climate Change Initiative Soil Moisture (ESA CCI Soil Moisture) project has produced a global soil moisture product for 38 year period from 1978 to 2016 combining both active and passive microwave observations. It is an international collaboration project between eight partners from Austria, the Netherlands, Switzerland, Finland, Ireland, and Norway. [11]

1.2.2 Soil frost

Soil freezing limits growing season and thus affects carbon cycle. It also has an effect on hydrologic cycle by preventing water from entering soil when in frozen state, as well as affecting surface energy balance, photosynthetic activity of vegetation and the activity of microbes in soil. Melting frost can break roads, but frozen ground also aids forest industry during winter by enabling soil to bear heavy machinery. In addition, global warming may cause melting permafrost, which could release methane to atmosphere and could thus accelerate climate change even more. Similar to the effects of moisture, freezing also affects permittivity of soil and thus the backscattering coefficient observed. Remote sensing of soil freeze has been studied using for example passive microwave radiometers [12, 13], SAR polarimetry [14], and scatterometers [15].

1.2.3 Vegetation

Vegetation is the basis of life on Earth. It absorbs carbon from atmosphere, prohibits erosion of soil, and provides food and other commodities to people and animals. Remote sensing can be used to classify vegetation, to survey crops, to map and monitor changes, and to detect damaged or stressed plants, due to diseases or pest insects. [1] Different aspects of vegetation can be observed using broad range of remote sensing instruments with varying wavelengths and observation methods. For example normalized difference vegetation index (NDVI) which is related to the amount of live green vegetation can be estimated using radiometer measurements [16] and leaf area index (LAI) using varying remote sensing methods both passive and active [17].

Usually remote sensing of vegetation is done using optical wavelengths. As they are sensitive to cloud conditions, also microwaves can be used. Vegetation also acts as an obstacle when trying to observe for example soil conditions and its effect on

backscattering needs to be taken into account when using radars. [18]

Chapter 2

Theory

2.1 Electromagnetic fields

Electromagnetic fields are described by Maxwell's equations. Inside matter with no free charge and no free current within the region, they become [19]

$$\begin{aligned} \nabla \cdot \mathbf{D} &= 0\,, \\ \nabla \cdot \mathbf{B} &= 0\,, \\ \nabla \times \mathbf{E} &= -\frac{\partial \mathbf{B}}{\partial t}\,, \\ \nabla \times \mathbf{H} &= \frac{\partial \mathbf{D}}{\partial t}\,, \end{aligned} \tag{2.1}$$

where $\mathbf{D}$ is the electric displacement, $\mathbf{E}$ is the electric field, $\mathbf{B}$ is the magnetic induction, and $\mathbf{H}$ is the magnetic field. In uniform isotropic linear medium [20]

$$\begin{aligned} \mathbf{D} &= \epsilon \mathbf{E}\,, \\ \mathbf{B} &= \mu \mathbf{H}\,, \end{aligned} \tag{2.2}$$

where ϵ is the electric permittivity and μ is the magnetic permeability.

2.2 Electromagnetic waves

In satellite remote sensing the distances between the source, the target and the detector are large, so radiation can usually be modeled as a plane wave. When time-harmonic plane waves are propagating in homogenous, linear, isotropic, and non-absorbing medium they have the same phase and oscillate in orthogonal directions

against each other and the direction of propagation. The equations for electric and magnetic fields are [21]

$$\begin{aligned} \mathbf{E} &= \mathbf{E}_0 e^{i(\mathbf{k}\cdot\mathbf{r}-\omega t)}\,, \\ \mathbf{H} &= \mathbf{H}_0 e^{i(\mathbf{k}\cdot\mathbf{r}-\omega t)}\,, \end{aligned} \tag{2.3}$$

or considering only the amplitude of real part

$$\begin{aligned} E &= E_0 \cos\left(\mathbf{k}\cdot\mathbf{r}-\omega t\right)\,, \\ H &= H_0 \cos\left(\mathbf{k}\cdot\mathbf{r}-\omega t\right)\,, \end{aligned} \tag{2.4}$$

where E_0 and H_0 are the amplitudes of electric and magnetic fields respectively, $\mathbf{k}$ is the wave vector, $\mathbf{r}$ is the radius vector, ω is the angular frequency, and t is time.

Wave vector $\mathbf{k}$ is a vector pointing to the direction of propagation of the wave. Its amplitude k is called wavenumber and it is the spatial frequency of the wave [19, 20]

$$k = \frac{2\pi}{\lambda} = \omega\sqrt{\mu\epsilon}\,, \tag{2.5}$$

where λ is the wavelength of the radiation in medium. Angular frequency ω is defined as

$$\omega = \frac{2\pi}{T} = 2\pi f\,, \tag{2.6}$$

where T is the period and f is the frequency of the radiation. Wavelength, frequency and speed of radiation are related to each other by equation

$$v = \lambda f\,, \tag{2.7}$$

and in vacuum $v = 2.99792458 \cdot 10^8$ m/s.

The direction of the oscillation of the electromagnetic waves is called polarization and it is defined by polarization vector $\hat{\mathbf{n}}$ which is perpendicular to the direction of propagation: [19]

$$\hat{\mathbf{n}} \cdot \hat{\mathbf{k}} = 0\,. \tag{2.8}$$

$\hat{\mathbf{n}}$ can be defined as a linear combination of two orthogonal components using polarization angle θ:

$$\hat{\mathbf{n}} = \cos\theta\ \hat{\mathbf{x}} + \sin\theta\ \hat{\mathbf{y}}\,. \tag{2.9}$$

2.3 Electromagnetic properties of matter

2.3.1 Permittivity and permeability

Permittivity tells us how a dielectric medium affects and is affected by an electric field. It is determined by how much the material reduces the effect of an outer electric field inside itself. This generally depends on the frequency of the field because the response within the material is not instant. Therefore permittivity of a non-linear medium is considered a complex function $\tilde{\epsilon}(f)$ and similarly to equation (2.2) it is defined by [19]

$$D_0 = \tilde{\epsilon}(f) E_0 \,, \tag{2.10}$$

where D_0 is the amplitude of the electric displacement field within the material, E_0 is the amplitude of the electrical field and f is the frequency of the electrical field. Permittivity is usually given as a relative permittivity compared to that of a vacuum [22]

$$\epsilon_r = \frac{\epsilon}{\epsilon_0} \,, \tag{2.11}$$

where $\epsilon_0 \approx 8.854 \cdot 10^{-12}$ F/m is the vacuum permittivity. Relative permittivity can be divided into real and imaginary parts

$$\epsilon_r = \epsilon_r' - i\epsilon_r'' \,, \tag{2.12}$$

where ϵ_r' is the real part and is related to the stored energy within the medium and ϵ_r'' is the imaginary part, which is related to the loss of energy within the medium. The effect of the imaginary part is usually small unless the frequency is close to a resonant frequency of the medium. [19]

Permeability

$$\mu = \mu_0 \left(1 + \chi_m\right) \,, \tag{2.13}$$

where, $\mu_0 = 4\pi \cdot 10^{-7}$ N/A^2 is the permeability of vacuum, and χ_m is the magnetic susceptibility. Susceptibility tells how a material is affected by a magnetic field. It is dimensionless, and for paramagnets the values are positive and for diamagnets they are negative. In this work, all media are considered to be non-magnetic so $\chi_m = 0$ and $\mu = \mu_0$. [19]

2.4 Interactions of electromagnetic waves with natural media

2.4.1 Extinction

An electromagnetic wave propagating inside a physical medium experiences a loss called extinction due to scattering and conduction losses. Extinction per unit length is called the extinction coefficient κ_e and it is the sum of absorption coefficient κ_a and scattering attenuation coefficient κ_s, so that

$$\kappa_e = \kappa_a + \kappa_s \,. \tag{2.14}$$

Power of the wave at depth z in a medium is [23]

$$P(z) = P(0+)e^{-\int_0^z \kappa_e(z')\mathrm{d}z'} \,, \tag{2.15}$$

where P(0+) is power just after the boundary layer of the medium and $\kappa_e(z')$ is extinction coefficient at depth z'. Penetration depth δ_p is defined when [23]

$$\frac{P(\delta_p)}{P(0+)} = \frac{1}{e} \,, \tag{2.16}$$

where $P(\delta_p)$ is power at depth δ_p and $e \approx 2.718$, or

$$\int_0^{\delta_p} \kappa_e(z)\mathrm{d}z = 1 \,. \tag{2.17}$$

If the extinction coefficient is constant throughout the medium then the relation simplifies as

$$\delta_p = \frac{1}{\kappa_e} = \frac{1}{\kappa_a + \kappa_s} \,. \tag{2.18}$$

2.4.2 Reflection and transmission

When a monochromatic plane wave encounters a boundary of two linear media free of surface charges and currents, part of it reflects back and part refracts to the second medium. At the boundary the normal components of $\mathbf{D}$ and $\mathbf{B}$, and the tangential components of $\mathbf{E}$ and $\mathbf{H}$ are continuous, as stated by

$$\begin{aligned} \mathbf{D}_{\perp i} + \mathbf{D}_{\perp r} &= \mathbf{D}_{\perp t} \,, \\ \mathbf{B}_{\perp i} + \mathbf{B}_{\perp r} &= \mathbf{B}_{\perp t} \,, \\ \mathbf{E}_{\parallel i} + \mathbf{E}_{\parallel r} &= \mathbf{E}_{\parallel t} \,, \\ \mathbf{H}_{\parallel i} + \mathbf{H}_{\parallel r} &= \mathbf{H}_{\parallel t} \,, \end{aligned} \tag{2.19}$$

where indices i, r, and t refer to incident, reflected and transmitted waves, respectively. [19]

From equations (2.19) it can be derived that the angle of incidence and the angle of reflection are equal

$$\theta_i = \theta_r \,. \tag{2.20}$$

This is also known as the law of reflection. For the transmitted angle we get

$$\frac{\sin\theta_t}{\sin\theta_i} = \frac{n_1}{n_2} \,, \tag{2.21}$$

which is known as the law of refraction or Snell's law. [19] n_1 and n_2 are the refractive indices of the two media in question and are defined by

$$n = \sqrt{\epsilon_r \mu_r} \tag{2.22}$$

where ϵ_r is the relative permittivity and μ_r is the relative permeability of the medium in question.

Reflection and transmission coefficients are defined as the ratio of amplitudes of reflected and incident irradiance and transmitted and incident irradiance, respectively. Assuming the permeabilities of both media are equal, for vertical polarization they are

$$\begin{aligned} \tilde{r}_\parallel &= \frac{E_{\parallel r}}{E_{\parallel i}} = \frac{\cos\theta_t - \frac{n_2}{n_1}\cos\theta_i}{\cos\theta_t + \frac{n_2}{n_1}\cos\theta_i} \,, \\ \tilde{t}_\parallel &= \frac{E_{\parallel t}}{E_{\parallel i}} = \frac{2\cos\theta_t}{\cos\theta_t + \frac{n_2}{n_1}\cos\theta_i} \,, \end{aligned} \tag{2.23}$$

and for horizontal polarization

$$\begin{aligned} \tilde{r}_\perp &= \frac{E_{\perp r}}{E_{\perp i}} = \frac{\cos\theta_i - \frac{n_2}{n_1}\cos\theta_t}{\cos\theta_i + \frac{n_2}{n_1}\cos\theta_t} \,, \\ \tilde{t}_\perp &= \frac{E_{\perp t}}{E_{\perp i}} = \frac{2\cos\theta_i}{\cos\theta_i + \frac{n_2}{n_1}\cos\theta_t} \,, \end{aligned} \tag{2.24}$$

These equations are known as Fresnel formulas. [24] The portion of reflected irradiance is called reflectance and is defined by

$$\begin{aligned} R_\parallel &= |\tilde{r}_\parallel|^2 \,, \\ R_\perp &= |\tilde{r}_\perp|^2 \,. \end{aligned} \tag{2.25}$$

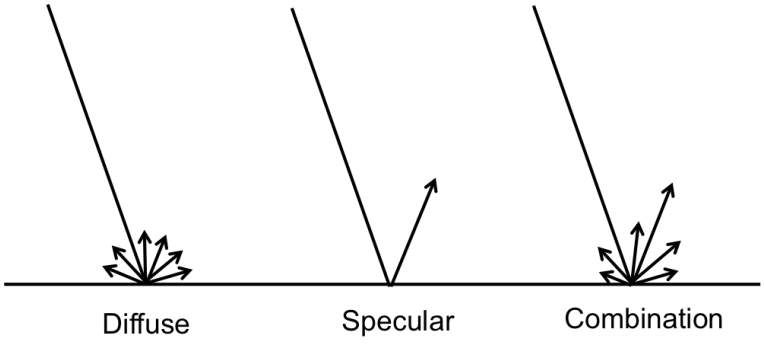

Figure 2.1: Various scattering patterns.

2.4.3 Scattering

The two ways to approximate scattering of an electromagnetic wave are surface scattering and volume scattering. Scattering from the boundary surface between two homogenous media is called surface scattering. Scattering inside a medium – either because the medium is inhomogenous or a mixture of materials – is referred to as volume scattering. In the boundary of the media some of the incident radiation is scattered from the surface and the rest is transmitted into the other medium. [23]

If scattered power is distributed to all directions, the scattering is called diffuse. Reflection is called specular scattering. Scattering can also be a combination of diffuse and specular components (see Figure 2.1).

Surface scattering strength is proportional to the relative complex dielectric constant of the surface. Angular scattering pattern is determined by surface roughness relative to wavelength. Smooth surfaces produce specular scattering and rough surfaces produce diffuse scattering.

Volume scattering is caused mainly by dielectric discontinuities inside a medium (see Figure 2.2). Scattering strength is proportional to these discontinuities and their density in the medium. Angular scattering pattern is determined by average dielectric constant and the size of inhomogenities relative to wavelength.

Backscattering refers to the amount of scattered energy that is scattered back to the incident wave direction. Its magnitude is determined by the magnitudes and angular patterns of possible surface and volume scattering components.

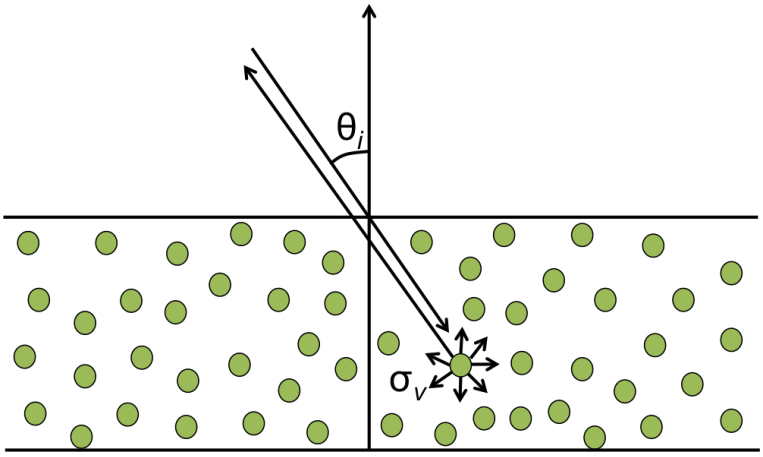

Figure 2.2: Schematic illustration of volume scattering σ_V with incidence angle θ_i.

2.5 Principle of radar measurement

When an antenna with gain G is transmitting with power P_t towards a scatterer at a distance R, the power density at the scatterer [23]

$$S_s = \frac{P_t G}{4\pi R^2} \,. \tag{2.26}$$

The total power affecting the scatterer is this power density multiplied by the effective receiving area of the scatterer:

$$P_{rs} = S_s A_{rs} \,. \tag{2.27}$$

As some of this power is absorbed in the scatterer, the total reradiated power is

$$P_{ts} = P_{rs}(1 - f_a) \,, \tag{2.28}$$

where f_a is the fraction absorbed. If we assume that the transmitting and receiving locations and antennas are same, the power density of scattered radiation at the receiver is

$$S_r = \frac{P_{ts} G_{ts}}{4\pi R^2} \,, \tag{2.29}$$

where G_{ts} is the gain of the scatterer in that direction. The power entering the receiver is affected by its effective aperture

$$P_r = S_r A_r \,, \tag{2.30}$$

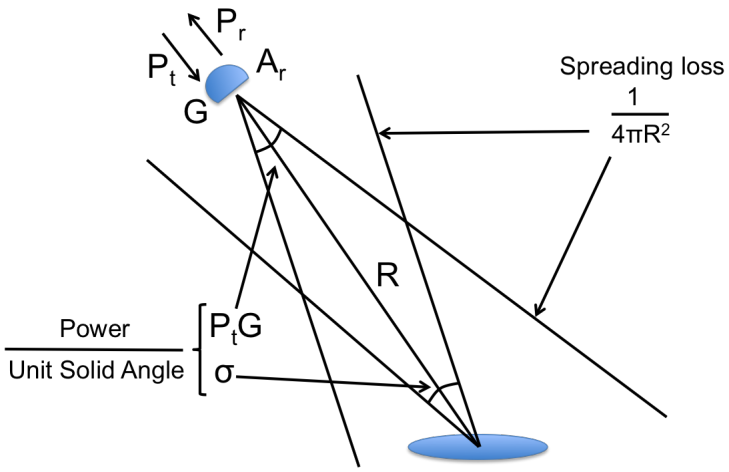

Figure 2.3: Schematic illustration of the radar equation. P_t and P_r are the transmitted and the received power respectively, G is the gain and A_r the effective aperture of the antenna, σ is the scattering cross-section of the scatterer, and R is the distance between the radar and the scatterer.

which combined with previous equations yields

$$P_r = \frac{P_t G A_r}{(4\pi)^2 R^4} A_{rs}(1 - f_a) G_{ts} \,. \tag{2.31}$$

Properties of scatterer are combined to scattering cross-section defined by

$$\sigma = A_{rs}(1 - f_a) G_{ts} \,, \tag{2.32}$$

and the effective aperture of an antenna is related to its gain by

$$A_r = \frac{\lambda^2 G}{4\pi} \,, \tag{2.33}$$

where λ is the wavelength. Thus the equation for the received power of an active instrument can be written as

$$P_r = \frac{P_t G^2 \lambda^2 \sigma}{(4\pi)^3 R^4} \,. \tag{2.34}$$

This equation is known as radar equation and main factors are illustrated in Figure 2.3. [25] Transmitting power P_t, gain G, and wavelength λ are properties of the radar, while the scattering cross-section σ is related to the properties of the scatterer.

The backscattering coefficient σ°, which used in this study, is expressed as the average of the ratio of the radar cross section σ and the area of the target A according

to equation

$$\sigma^\circ = \langle \frac{\sigma}{A} \rangle \,. \tag{2.35}$$

Measurements are often expressed on a logarithmic scale. The conversion is calculated with equation [26]

$$\sigma^\circ_{dB} = 10 \cdot log_{10}\sigma^\circ \,. \tag{2.36}$$

The electromagnetic signal transmitted by a radar is polarized either horizontally or vertically. Radars also observe horizontally and vertically polarized reflections separately. Observing horizontally polarized reflection of a horizontal signal is called like-polarized mode and the resulting image is referred to as the HH image. Observing vertically polarized reflection of a horizontal signal is called cross-polarized mode with HV image. Same also applies when transmitted signal is polarized vertically and the results are then referred to as the VV and VH images. [1]

2.6 Methods for modelling backscatter

To interpret backscattering measurements we need to understand how they relate to physical parameters involved. This requires models that explain scattering in the particular case we are examining. These models can be based purely on theory or empirical measurements or they can be a combination. In last case they are called semi-empirical models.

2.6.1 Surface scattering

Surface scattering of slightly rough surfaces can be modeled using the small perturbation method, and rough surfaces with large surface curvature using the Kirchhoff approximation. Methods that combine both cases are for example the small slope approximation and the integral equation model (IEM), which has been improved to the advanced integral equation model (AIEM). [27]

2.6.2 Volume scattering

Volume backscattering can be modeled by considering uniformly distributed identical scatterers (“water cloud”). Multiple scattering can be ignored if the density of

scatterers is sparse. Volume backscattering coefficient σ_v ($\mathrm{m^2 m^{-3}}$) and extinction coefficient κ_e ($\mathrm{m^{-1}}$) are thus [23]

$$\sigma_v = N\sigma_b \,, \tag{2.37}$$

$$\kappa_e = NQ_e \,, \tag{2.38}$$

where N ($\mathrm{m^{-3}}$) is the number of scattering particles in unit volume, σ_b ($\mathrm{m^2}$) is the backscattering cross-section of one particle and Q_e ($\mathrm{m^2}$) is the extinction cross-section of one particle.

Power upon horizontal area A is [23]

$$P_A = SA\cos\theta \,, \tag{2.39}$$

where S is the power density of an incident plane wave and θ is the incident angle.

The attenuation between the surface and the scattering layer can be calculated from (2.15) when extinction coefficient κ_e is constant by

$$P(z) = P(0+)e^{-\kappa_e z} \,. \tag{2.40}$$

Total volume backscatter is calculated by integrating the backscatter of each layer dz for the distance $\frac{h}{\cos\theta}$, where h is the vertical height of the scattering medium. The attenuation occurs both ways, so the backscattered power at a distance R is [23]

$$P_r = \frac{P_A}{4\pi R^2}\int_0^{\frac{h}{\cos\theta}} \sigma_v e^{-2\kappa_e z}\mathrm{d}z = \frac{SA\cos\theta}{4\pi R^2}\frac{\sigma_v}{-2\kappa_e}e^{-2\kappa_e z}\Big|_0^{\frac{h}{\cos\theta}} = \frac{\sigma_v SA\cos\theta}{8\pi\kappa_e R^2}\left[1-e^{-\frac{2\kappa_e h}{\cos\theta}}\right] . \tag{2.41}$$

Backscattering coefficient is determined as a fraction of the received and incident powers [23]

$$\sigma_v^\circ(\theta) = \frac{4\pi R^2 P_r}{AP_i} = \frac{4\pi R^2 \frac{\sigma_v SA\cos\theta}{8\pi\kappa_e R^2}\left[1-e^{-\frac{2\kappa_e h}{\cos\theta}}\right]}{AS} = \frac{\sigma_v\cos\theta}{2\kappa_e}\left[1-e^{-\frac{2\kappa_e h}{\cos\theta}}\right] . \tag{2.42}$$

Scattering from individual spherical scatterers can be modeled using Mie scattering or for scatterers that are small compared to wavelength using Rayleigh scattering which is an approximation of Mie scattering. For scatterers that are large compared to wavelength geometrical optics approximation can be used. [28]

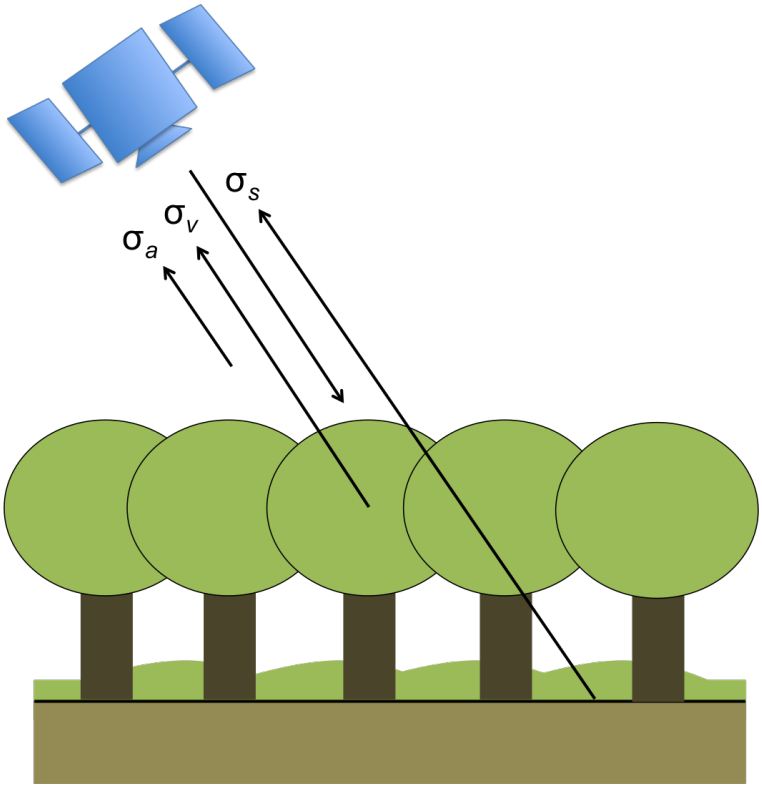

Figure 2.4: Scattering from forested terrain, showing contributions from air σ_a, vegetation σ_v, and soil σ_s.

2.7 Modelling backscatter of forested terrain

Backcattering from forested terrain consists of several contributions, the main ones being scattering from air σ_a, vegetation σ_v, and soil σ_s. Figure 2.4 shows a schematic picture of these three scattering instances.

Scattering in atmosphere is caused by particles with size of the same magnitude as observing wavelength. For microwaves water drops are the most significant ones, and can be modeled using Mie-scattering. Gas molecules cause only absorption for microwaves. [28] For wavelengths used in this study both of these effects can be neglected.

A simple method to model scattering from vegetation is to use the water cloud model presented in chapter 2.6.2 which assumes that scattering is caused by uniformly distributed identical scatterers. More complicated models have also been developed, for example Michigan Microwave Canopy Scattering Model (MIMICS)

that accounts scattering from leaves, branches and trunks. [29]

For modeling scattering from bare soil, semi empirical models like Oh et al. [30] and Dubois et al. [31] have been developed. During winter the snow cover provides additional source of both surface and volume scattering, and can be modeled as a layer of randomly distributed dielectric spherical scatterers between two rough surfaces. [32]

The relative weight of scattering from the vegetation and from the ground depends on factors like penetration depth, the height of the canopy, the frequency of the radar and the incidence angle. With large incidence angles the scattering from the vegetation is more dominant, as the microwaves need to travel longer distance through it, whereas close to nadir the scattering from the ground is equally important. The penetration depth in the vegetation depends on the frequency, the geometry and the moisture of the canopy, and also the vegetation volume fraction, and it is usually at least some meters for microwaves. The penetration depth in soil depends on the soil moisture content and for microwaves at C-band in loamy soil the penetration depth varies from 10 centimeters to 1 centimeter for volumetric moisture contents of 0 g cm^{-3} and 0.4 g cm^{-3} respectively. [23]

The penetration depth of microwaves in snow depends heavily of the water content of the snowpack. For dry snow at C-band it can be over 10 meters but drops to less than a meter for volumetric liquid water content of 1 % and to only 10 centimeters for liquid water content of 5 %. [23] This means that the effect of snow for satellite retrievals depends heavily on temperature.

Chapter 3

Data

3.1 ASCAT

ASCAT is an abbreviation for Advanced SCATterometer and is an instrument on-board MetOp-satellite. First satellite in MetOp (Meteorological Operational) series called MetOp-A was launched by ESA and the European Organisation for the Exploitation of Meteorological Satellites (Eumetsat) in October 2006 from the Baikonur Cosmodrome in Kazakhstan. The next one called MetOp-B was launched on 17th September 2012. Third one, MetOp-C is planned to be launched in 2018. [33]

The MetOp satellites are placed on Sun-synchronous orbits so that they pass the same points on Earth's surface every day at the same time and the same position relative to the Sun. The mean altitude of the orbit is approximately 817 kilometers and orbital period is 101 minutes. The inclination of the orbit is 98.7 degrees and thus it passes close to Earth's poles.

ASCAT is a C-band (5.255 GHz) pulse radar. One of its purposes was to study sea winds by measuring the backscattering coefficient of sea surface. ASCAT has two three-meter long antenna arms at fixed positions $\pm 135^\circ$ with respect to the flight direction of the satellite. Both arms have two antennae and two more are attached to the satellite body totaling six antennae. These antennae make three sequential observations on both sides of the satellite consisting of fore-, mid- and aft-beam measurements. There are two separate swaths being measured simultaneously, 550 kilometers wide each. Near global coverage is achived in five days. [34]

Table 3.1: Properties of MetOp-A -satellite and ASCAT-instrument.

Satellite

Property	Value
Total mass	4093 kg
Size	17.6 m × 6.5 m × 5.2 m
Mean altitude	817 km
Recurrent period	29 days (412 orbits)
Orbital period	101 min
Inclination	98.7°

Instrument

Property	Value
Frequency	5.255 GHz
Polarization	VV
Measurement angle	25°-65°
Antenna	2 × 6 antennas

Table 3.2: Properties of Envisat-satellite and ASAR-instrument.

Satellite

Property	Value
Total mass	8200 kg
Size	26 m × 10 m × 5 m
Mean altitude	800 km
Recurrent period	35 days (501 orbits)
Orbital period	101 min
Inclination	98.55°

Instrument

Property	Value
Frequency	5.331 GHz
Polarization	VV, HH, VV+HH, HH+HV, or VV+VH
Measurement angle	15-45°
Antenna	active phased array, aperture 10 m × 1.3 m

3.2 ASAR

ASAR is an acronym for Advanced Synthetic Aperture Radar and it was an instrument onboard of Envisat-satellite. Envisat (Environmental Satellite) was launched by ESA on 1st March 2002 from the Guyana Space Centre in Kourou, French Guyana. It is on a Sun-synchronous polar orbit at an altitude of 790 km and it orbits the Earth in 101 minutes with a repeat cycle of 35 days. Envisat carried a total of nine observational instruments, from which ASAR was one. Contact to Envisat was lost on 8th April 2012 and the mission had to be ended. [35]

3.3 Test setup

A time serie of five years from July 2007 to June 2012 was investigated (ASAR data ended already in April 2012 due to satellite malfunction). For ASCAT there were 4 016 individual backscattering (σ°) measurements from 1820 dates during this

period, all VV-polarized. For ASAR there were 499 individual backscattering measurements from 494 dates, of which 140 were VV-polarized and 359 HH-polarized. ASCAT data used in this study was provided by Vienna Technical University and ASAR data was provided by Gamma Remote Sensing. The spatial resolution of the ASCAT data was approximately 12 km $\times$ 12 km and for ASAR data it was 1/720 degrees, which at the Sodankylä area means approximately 150 m $\times$ 60 m.

For ASAR retrieval forest stem volume data provided by Natural Resources Institute Finland (former Finnish Forest Research Institute) were used. These data are based on multi-source national forest inventory and combine field measurements with remote sensed data, land-use maps, elevation models, and other digital data sources. [36]

The satellite products were compared against *in situ* measurements in Sodankylä in Northern Finland. Finnish Meteorological Institute's (FMI) Arctic research station is located in Sodankylä and gathers information on varying environmental parameters including soil moisture and temperature. Sodankylä region represents a boreal forest environment with 71% of surrounding landscape being forested. 18% of the area is covered by open and forested bogs. [6] Soil permittivity is measured using Delta-T Devices ThetaProbe ML2x instruments at 2 cm and 10 cm depths. Soil temperature is measured using Vaisala QMT103 Soil Temperature Probes at 2 cm depth. Soil frost is measured manually three times in a month by Finnish Environment Insitute (SYKE) using frost tubes in different land cover classes (forest, open area and wetland) within the area. [37] The tubes are made of Chlorinated Polyvinyl Chloride and filled with a mixture of water and food colorant that changes when frozen which then allows the frost depth to be measured manually. [13] Snow depth is measured automatically with Campbell Scientific SR50 instrument, which is an ultrasonic distance sensor. The location of the station is 67.4°N, 26.6°E. For ASCAT the data for one pixel surrounding this location were used. For ASAR, only data within this ASCAT pixel were used.

Figure 3.1 shows the time series of both ASCAT and ASAR backscatter data for the whole time period investigated. ASCAT data are for one pixel and ASAR shows the average within said pixel. Only measurements covering at least 68% of the ASCAT pixel were included so that they would be representative of the area, but would not leave out too many observation days. Both satellite datasets demonstrate

high variance in observed backscattering. Seasonal variation can be seen in both ASCAT and ASAR observations, but it is more defined in ASCAT data. The highest backscatter values are observed during summertime. In autumn, during the freezing period, the average backscatter values are lower than during summer. In winter snow cover increases the backscattering compared to autumn, but in average the level is still lower than during summer. During spring when the snow is melting the backscatter exhibits low values similar to the autumn period.

Figures 3.2 and 3.3 show ASAR backscatter for 2nd October and 13th December 2011. On the left side the total area of one degree times one degree is shown and on the right side is the area representing the area of ASCAT pixel.

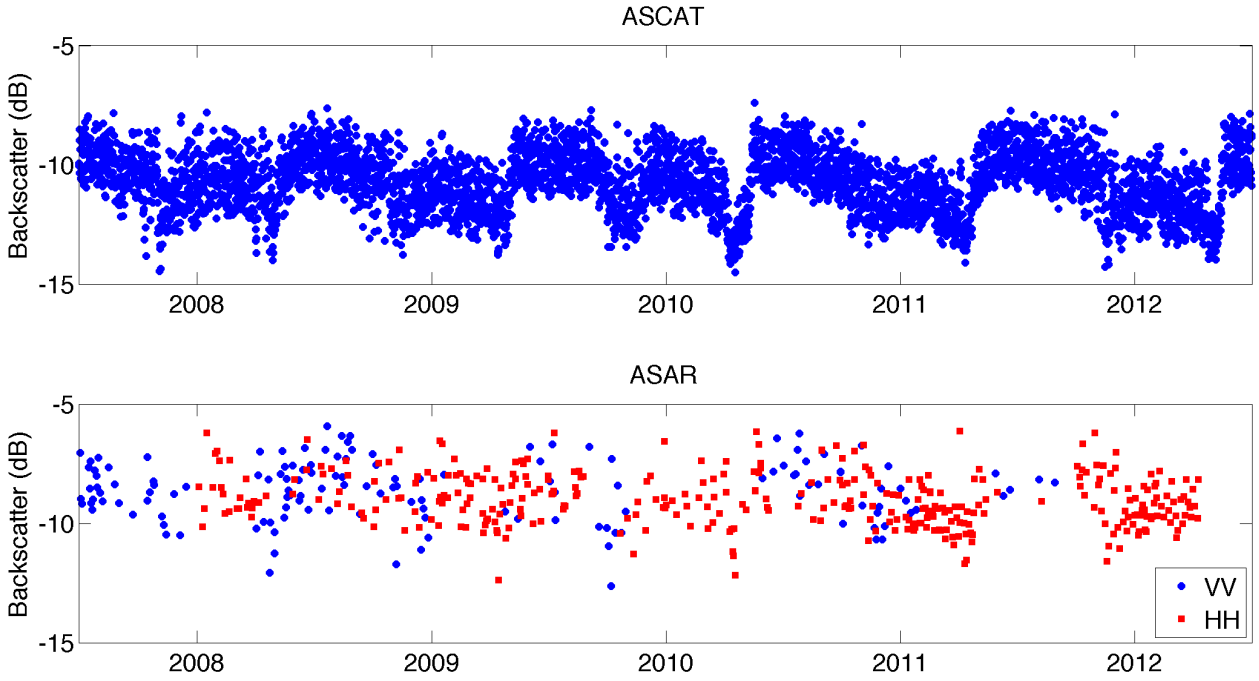

Figure 3.1: Backscatter time series of ASCAT and ASAR observations for years 2007-2012. Blue circles indicate vertical (VV) and red squares horizontal (HH) polarization.

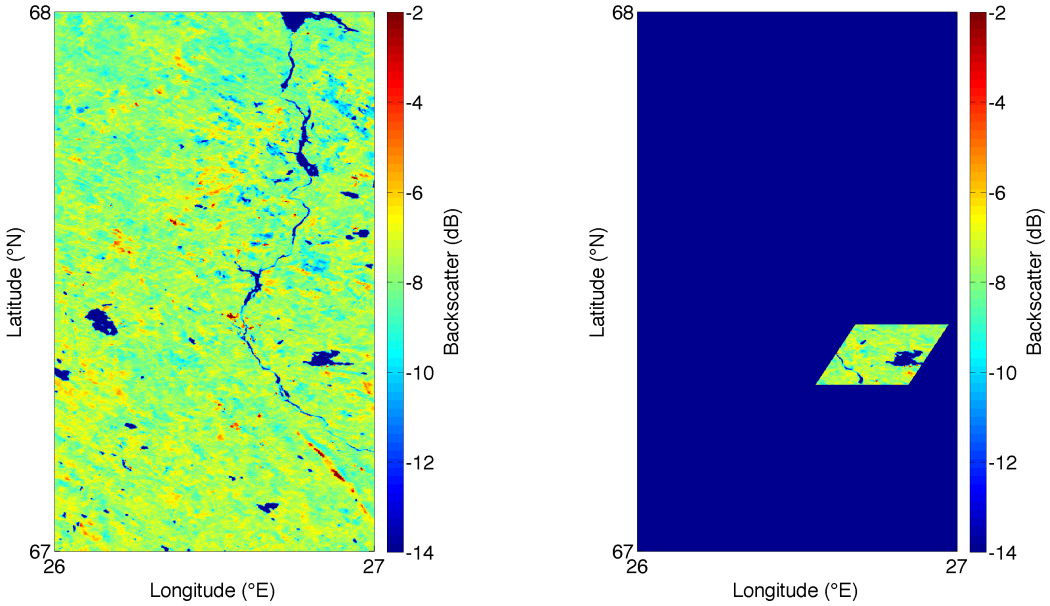

Figure 3.2: ASAR backscatter on 2nd October 2011. Total area on the left, and the area representing the ASCAT pixel on the right.

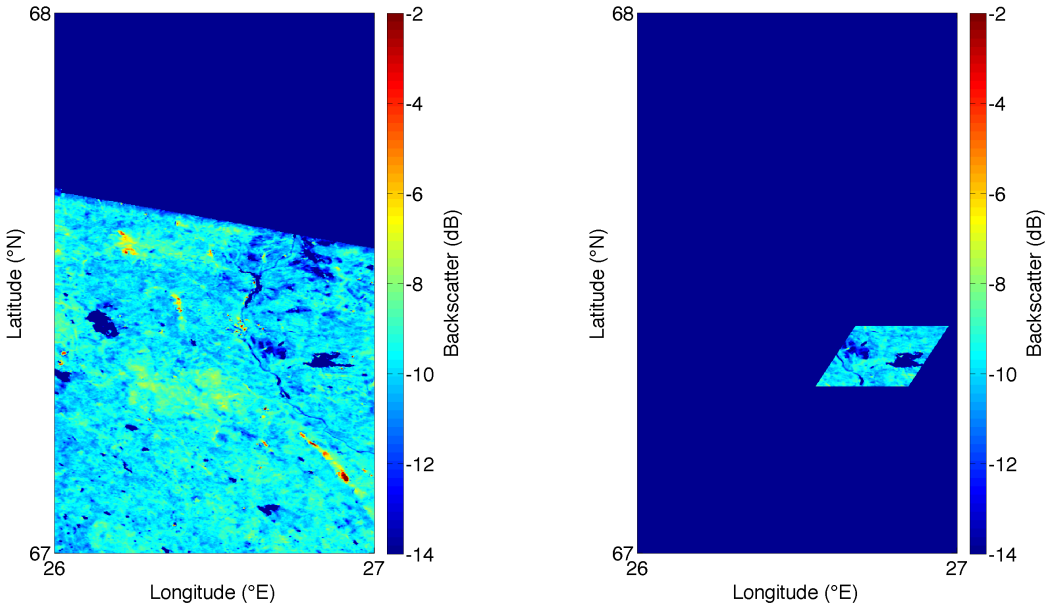

Figure 3.3: ASAR backscatter on 13th December 2011. Total area on the left, and the area representing the ASCAT pixel on the right.

Chapter 4

Methods

4.1 Forward model for backscattering

A semiempirical model is used to describe the backscattering properties of forested land as a combination of scattering from forest canopy and ground. The backscattering coefficient of forested land can be written as [7]

$$\sigma^\circ(V, \theta, \kappa_{can}, \epsilon_{soil}) = \sigma^\circ_{can}(V, \theta, \kappa_{can}) + t^2(V, \theta, \kappa_{can}) \cdot \sigma^\circ_{soil}(\epsilon_{soil}, \theta, f, s_g)\,, \qquad (4.1)$$

where σ°_{can} is the backscattering coefficient of the forest canopy, σ°_{soil} is the backscattering from the ground (described using Oh-model, [30]), t^2 is the two-way forest canopy transmissivity, κ_{can} is the extinction coefficient of forest canopy, ϵ_{soil} is the relative permittivity of soil, V is the forest stem volume (in m^3/ha), θ is the angle of incidence, f is the radar frequency, and s_g is the surface roughness of the ground. σ°_{soil} includes trunk-ground reflection, but its magnitude has been found to be marginal in boreal forests in C-band. [7] A schematic illustration of the model is presented in Figure 4.1.

4.1.1 Forest canopy

Scattering from forest canopy can be modeled using water cloud model from section 2.6.2. The transmissivity of the forest canopy can be written as

$$t^2 = exp\left(\frac{-2 \cdot \kappa_{can} \cdot V}{\cos\theta}\right)\,, \qquad (4.2)$$

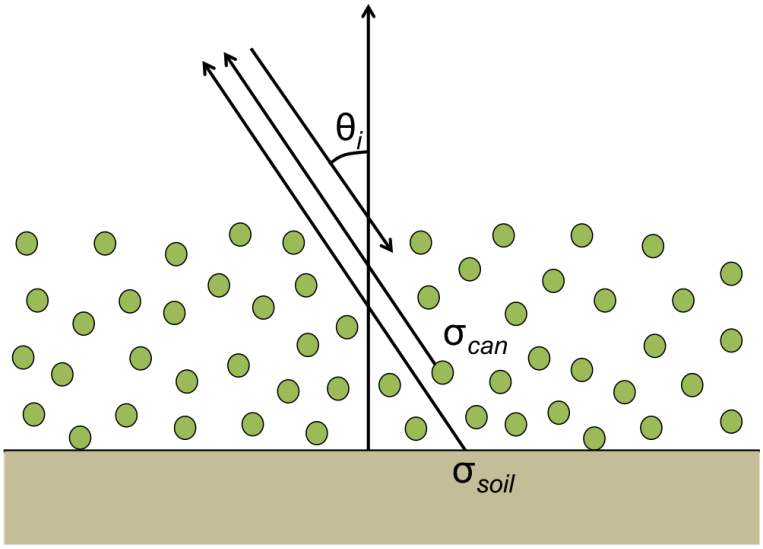

Figure 4.1: Schematic illustration of the backscattering model for forested land. σ_{can} is the backscattering coefficient of canopy, σ_{soil} is the backscattering coefficient of soil, and θ_i is the incidence angle.

where κ_{can} is an empirical coefficient for forest canopy extinction (ha/m^3). The canopy backscattering coefficient can be written as

$$\sigma^{\circ}_{can} = \frac{\sigma_V}{2\kappa_{can}} \cdot \cos\theta \cdot (1 - t^2)\,, \tag{4.3}$$

where σ_V is an empirically defined volume backscattering coefficient in the canopy (ha/m^3), and related to the volumetric water content of the canopy. [38]

According to [38] the influence of parameters κ_{can}, σ_V, and σ°_{soil} in equations (4.1)–(4.3) can be reduced into two empirical coefficients (assuming that $\sigma_V \sim m^2_{can}$ and $\kappa_{can} \sim m_{can}$, where m_{can} is the volumetric water content of the canopy) that can be estimated using reference data available from the study region. For C-band measurements for test site in the Tuusula region in Southern Finland used in that study, the equation (4.1) could be rewritten as

$$\begin{aligned}\sigma^{\circ}(V,\theta) = 0.131 \cdot a \cdot \cos\theta \left(1 - exp\left(-5.12 \cdot 10^{-3} \cdot \frac{a \cdot V}{\cos\theta}\right)\right) \\ + b \cdot exp\left(-5.12 \cdot 10^{-3} \cdot \frac{a \cdot V}{\cos\theta}\right)\,,\end{aligned} \tag{4.4}$$

where parameter a is related to the volumetric water content of the canopy and is close to 1 in dry conditions, and parameter $b \equiv \sigma^{\circ}_{soil}$.

4.1.2 Soil

The backscattering coefficient of the soil σ°_{soil} is acquired using the empirical soil scattering model by Oh et al. [30] which describes backscattering dependence on permittivity and surface roughness. According to the model the backscattering coefficient of soil at different polarizations is

$$\sigma^\circ_{vv}(\theta, \epsilon_r, ks) = \frac{g \cos^3 \theta}{\sqrt{p}} \cdot [\Gamma_v(\theta) + \Gamma_h(\theta)] \,, \tag{4.5}$$

$$\sigma^\circ_{hh}(\theta, \epsilon_r, ks) = g\sqrt{p} \cos^3 \theta [\Gamma_v(\theta) + \Gamma_h(\theta)] \,, \tag{4.6}$$

and

$$\sigma^\circ_{hv}(\theta, \epsilon_r, ks) = q \cdot \sigma^\circ_{vv}(\theta, \epsilon_r, ks) \,, \tag{4.7}$$

where

$$g = 0.7 \left[1 - e^{-0.65(ks)^{1.8}}\right] \,, \tag{4.8}$$

$$p = \frac{\sigma^\circ_{hh}}{\sigma^\circ_{vv}} = 1 - \left(\frac{2\theta}{\pi}\right)^{\frac{1}{3\Gamma_0}} \cdot e^{-ks} \,, \tag{4.9}$$

$$q = \frac{\sigma^\circ_{hv}}{\sigma^\circ_{vv}} = 0.23\sqrt{\Gamma_0}\left(1 - e^{-ks}\right) \,, \tag{4.10}$$

θ is the incidence angle and ks (where $k = 2\pi/\lambda$ is the wave number and s is the root-mean-square height) is roughness.

Refractive index of a medium is given by equation (2.22). In this case ϵ_r is the relative permittivity of soil and μ_r is approximately one because soil is considered non-magnetic at the wavelengths involved. Thus

$$n_{soil} = \sqrt{\epsilon_r} \,, \tag{4.11}$$

and according to equations (2.23)–(2.25) the Fresnel reflectivity of the surfaces at nadir

$$\Gamma_0 = \left|\frac{n_{air} - n_{soil}}{n_{air} + n_{soil}}\right|^2 = \left|\frac{1 - \sqrt{\epsilon_r}}{1 + \sqrt{\epsilon_r}}\right|^2 \,, \tag{4.12}$$

the Fresnel reflectivity for horizontal polarization

$$\Gamma_h = \left|\frac{n_{air}\cos\theta - n_{soil}\sqrt{1 - \left(\frac{n_{air}}{n_{soil}}\sin\theta\right)^2}}{n_{air}\cos\theta + n_{soil}\sqrt{1 - \left(\frac{n_{air}}{n_{soil}}\sin\theta\right)^2}}\right|^2 = \left|\frac{\cos\theta - \sqrt{\epsilon_r - \sin^2\theta}}{\cos\theta + \sqrt{\epsilon_r - \sin^2\theta}}\right|^2 \,, \tag{4.13}$$

and the Fresnel reflectivity for vertical polarization

$$\Gamma_v = \left| \frac{n_{soil}\cos\theta - n_{air}\sqrt{1-\left(\frac{n_{air}}{n_{soil}}\sin\theta\right)^2}}{n_{soil}\cos\theta + n_{air}\sqrt{1-\left(\frac{n_{air}}{n_{soil}}\sin\theta\right)^2}} \right|^2 = \left| \frac{\epsilon_r\cos\theta - \sqrt{\epsilon_r - \sin^2\theta}}{\epsilon_r\cos\theta + \sqrt{\epsilon_r - \sin^2\theta}} \right|^2 . \quad (4.14)$$

4.2 Inversion of the forward model

Inversion of the forward model (4.1) was made using the method of least squares. The solution was found by minimizing the sum of the squares of the difference between measurements and their predicted values. [39] The cost function took the form [7]

$$\sum_{i=1}^{N} \left[\sigma^\circ_{model,i}\left(\theta, V, \epsilon_{soil}, \kappa_{can}\right) - \sigma^\circ_{measured,i} \right]^2 , \quad (4.15)$$

where σ°_{model} is the backscatter coefficient provided by the forward model, and $\sigma^\circ_{measured}$ is the measured backscatter coefficient from satellite observations.

4.2.1 ASCAT

ASCAT instrument has three antennas providing three separate measurements with varying incidence angles so the cost function becomes

$$\sum_{i=1}^{N} \left[\sigma^\circ_{model}\left(\theta_i, V, \epsilon_{soil}, \kappa_{can}\right) - \sigma^\circ_{measured,i} \right]^2 , \quad (4.16)$$

where measurements with different angles are used to find permittivity values when forest volume is considered to be constant within observed area. Figure 4.2 shows an example for 2nd October 2011 when the soil is thawed and Figure 4.3 shows an example for 13th December 2011 when the soil is frozen. Backscattering coefficient is shown as a function of incidence angle. Blue circles indicate the ASCAT measurements with solid green line showing the backscattering model fitted to them to find soil permittivity estimate. The permittivity estimate obtained is the absolute value of the relative permittivity of soil. Dashed blue lines represent modeled backscatter with varying soil permittivity values. $\sigma^\circ_\perp$ shows the modeled backscattering at nadir i.e. when incidence angle is zero and look direction is perpendicular to the ground. The values for soil permittivity estimate and modeled backscatter at nadir are lower when the soil is frozen than when it is thawed.

As forward and backward facing beams have the same incidence angle, they were weighted only half of that of the middle beam each. Also as there were effectively only two different measurements, the extinction coefficient of the forest canopy was considered to stay constant.

4.2.2 ASAR

ASAR provides images with much better resolution than ASCAT, but with only one measurement per pixel with constant angle. Thus the cost function used for ASCAT (4.16) is not applicable. Instead, varying stem forest volume between adjacent pixels can be utilized. This requires that several pixels are considered to have the same soil permittivity and canopy extinction coefficient values. The cost function becomes

$$\sum_{i=1}^{N} w_i \left[\sigma^{\circ}_{model}\left(\theta, V_i, \epsilon_{soil}, \kappa_{can}\right) - \sigma^{\circ}_{measured,i}\right]^2, \tag{4.17}$$

where different forest stem volume values are used to find permittivity and canopy extinction coefficient while incidence angle is constant. w_i is an areal weighing factor of forest stem volume class i obtained by [40]

$$w_i = \frac{A_i}{\sum_{j=1}^{N} A_j} \tag{4.18}$$

where A_i denotes the total area of forests representing the stem volume class i. Figure 4.4 shows an example for 2nd October 2011 when the soil is thawed and Figure 4.5 shows an example for 13th December 2011 when the soil is frozen. Backscattering coefficient is shown as a function of stem volume. Blue circles indicate the median ASAR measurements for different stem volume classes accompanied by error bars showing standard error. Solid green line shows the backscattering model fitted to measurements to find estimate for the absolute value of the relative permittivity of soil. Dashed blue lines represent modeled backscatter with varying soil permittivity values. σ°_{g} shows the modeled backscatter when stem volume is zero indicating thus the backscattering coefficient of bare ground. Similar to ASCAT the values for soil permittivity estimate and modeled backscatter of bare ground are lower when the soil is frozen than when it is thawed.

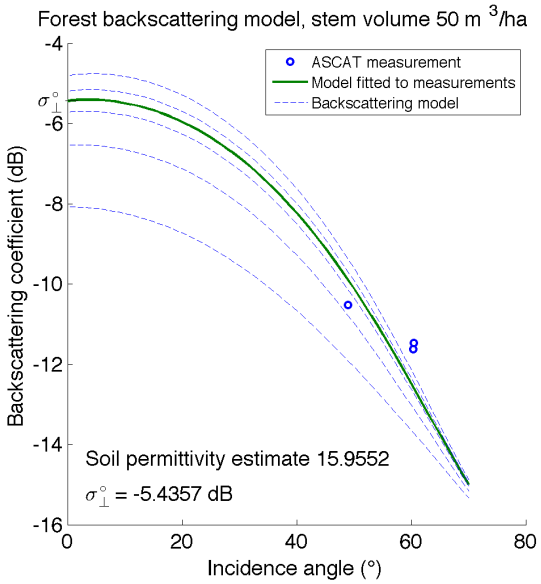

Figure 4.2: Backscatter model for ASCAT measurements on 2nd October 2011. Dashed blue lines represent the backscattering model with soil permittivity values of 6, 10, 14, 18, and 22, from the lowest line to the topmost one respectively. $\sigma^{\circ}_{\perp}$ is the modeled backscattering at nadir.

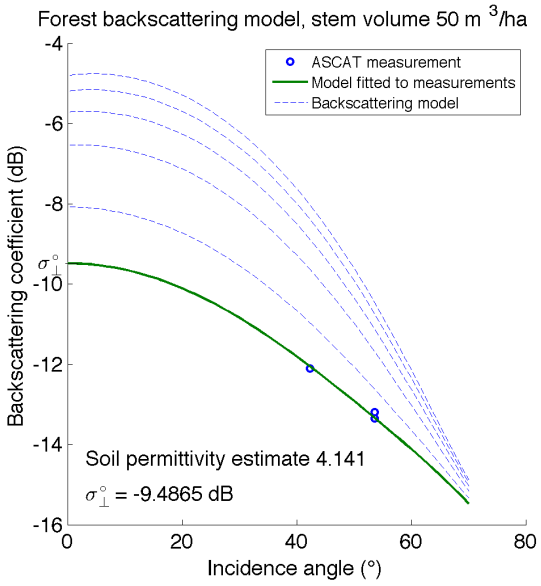

Figure 4.3: Backscatter model for ASCAT measurements on 13th December 2011. Dashed blue lines represent the backscattering model with soil permittivity values of 6, 10, 14, 18, and 22, from the lowest line to the topmost one respectively. $\sigma^{\circ}_{\perp}$ is the modeled backscattering at nadir.

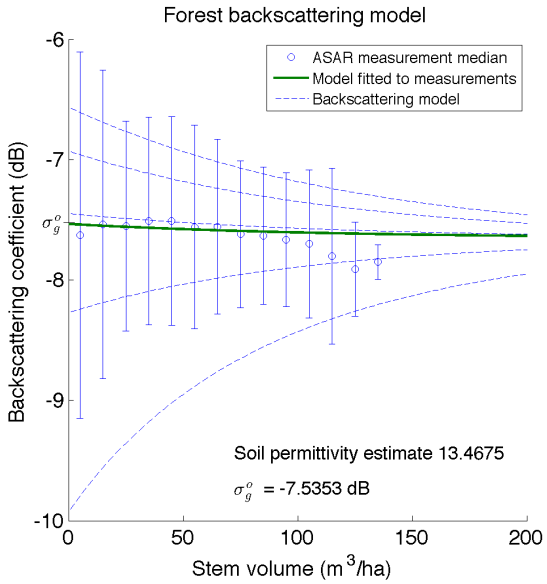

Figure 4.4: Backscatter model for ASAR measurements on 2nd October 2011. Dashed blue lines represent the backscattering model with soil permittivity values of 6, 10, 14, 18, and 22, from the lowest line to the topmost one respectively. σ_g° is the backscattering coefficient of bare ground.

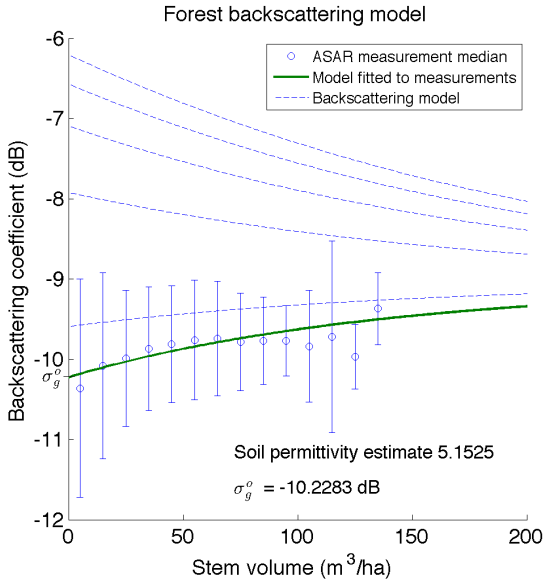

Figure 4.5: Backscatter model for ASAR measurements on 13th December 2011. Dashed blue lines represent the backscattering model with soil permittivity values of 6, 10, 14, 18, and 22, from the lowest line to the topmost one respectively. σ_g° is the backscattering coefficient of bare ground.

4.3 Soil frost

Freezing changes the dielectric properties of soil so that permittivity of frozen soil is lower than that of non-frozen soil. [41] This means that a simple method to determine the freezing of the soil from satellite retrieval is to consider the soil to be frozen when the permittivity estimate falls below a specific threshold value.

4.4 Error estimates

The average difference between two datasets is calculated by

$$\sum_{n=1}^{N} \frac{x_n - y_n}{N} = \bar{x} - \bar{y}\,, \tag{4.19}$$

where x_n and y_n are the corresponding points, N is the length of the datasets to be compared, and $\bar{x}$ and $\bar{y}$ are the mean values of the datasets. Positive difference means that the values of x are on average larger than the values of y and negative means that the values of y are on average larger than the values of x. When comparing satellite retrievals with *in situ* measurements this difference is called bias.

The standard deviation (STD) of a dataset is the root of the average squared deviation from the mean. It is related to the spread of the data and calculated by [39]

$$\sqrt{\sum_{n=1}^{N} \frac{(x_n - \bar{x})^2}{N}}\,. \tag{4.20}$$

Root mean square error (RMSE) is the standard deviation of the difference between two datasets, calculated by

$$\sqrt{\sum_{n=1}^{N} \frac{(x_n - y_n)^2}{N}}\,. \tag{4.21}$$

To compare two datasets without the effect of the bias between them, unbiased root mean square error can be used, calculated by [42]

$$\sqrt{\sum_{n=1}^{N} \frac{\left[(x_n - \bar{x}) - (y_n - \bar{y})\right]^2}{N}}\,, \tag{4.22}$$

Root mean square error gives always a positive value with the dimension of the datasets.

Correlation means that there is a linear relationship between two variables and correlation coefficient is the measure of the strength of the correlation between two datasets. The most common one is the Pearson product-moment coefficient of correlation, calculated by [43]

$$\frac{\sum_{n=1}^{N}(x_n - \bar{x})(y_n - \bar{y})}{\sqrt{\sum_{n=1}^{N}(x_n - \bar{x})^2}\sqrt{\sum_{n=1}^{N}(y_n - \bar{y})^2}}, \tag{4.23}$$

Pearson correlation coefficient measures linear correlation, and gets values between -1 and 1. Value of 0 means that there is no linear correlation between the variables and the closer the absolute value of the coefficient is to one the stronger the correlation is.

Chapter 5

Results and discussion

5.1 Time series

Figures 5.1–5.5 show time series for ASCAT and ASAR soil permittivity retrievals combined with *in situ* soil permittivity, soil temperature, snow depth, and soil frost measurements for five years from July 2007 to July 2012, centered around winter periods. ASCAT retrieval is shown with both daily and weekly values, ASAR with only daily values due to its sparser temporal resolution. Weekly values are calculated as a 7 day moving average, using the day in question ± 3 days as the time window. Both satellite retrievals and *in situ* measurements are absolute values of the relative soil permittivity.

At the start of November 2007 in Figure 5.1 weekly ASCAT retrieval drops around the same time as soil temperature and *in situ* permittivity. Snow and soil frost seem to also onset around the same time. In ASAR retrieval the change is more subtle. The start of the winter has been quite warm. In December 2007 the temperature increases back to zero after initial freezing and this can be also seen in the *in situ* permittivity measurements, but not in satellite retrievals because of the effect of snow cover. In January 2008 the temperature drops clearly below zero and the soil frost also gets much deeper.

At the start of November 2008 in Figure 5.2 the soil temperature drops slightly below zero and there are similar drops in both satellite permittivity retrievals as well as in *in situ* permittivity. In the middle of the November 2008 the temperature has increased back to zero and there is an increase in all permittivity measurements

and retrievals. After that the temperature and permittivities drop again and there is also a slight increase in soil frost depth. Temperatures decrease in January 2009 and there is also a clear increase in soil frost depth.

The start of winter in 2009-2010 in Figure 5.3 has been very warm staying close to zero from October to mid-December even though snow has fallen in October. This has resulted to minimal soil frost until December when the temperature has dropped below zero. *In situ* permittivity does not show any signs of freezing until December but weekly ASCAT retrieval shows a clear drop already at October, as does ASAR retrieval as well. These are probably caused by the snow cover.

In 2010-2011 in Figure 5.4 the situation is more clear. Even though the snow has fallen at the end of October 2010, soil temperature did not drop below zero until November and also all permittivities show a decline at that same point. Also the depth of soil frost does not increase until mid November.

Summer 2011 in Figure 5.5 has fewer ASAR measurements than other years and there is also more noise present. *In situ* permittivity has less variability than previous years. Temperature drops below zero at mid-November and this can be seen as a drop in both satellite retrievals. This moment also shows first snowfall and the onset of soil frost. At the end of November temperature rises to zero twice with a short colder period between. Both daily permittivity retrievals as well as *in situ* measurements show higher values when temperature is near zero and and lower when it is colder.

Throughout all years, daily ASCAT retrieval has a lot of noise during summers, whereas ASAR retrieval is more consistent. Both satellite retrievals show higher overall level than *in situ* measurements. During autumn periods the satellite retrievals seem to decline around the same time the soil temperature approaches zero. During winters the snow cover increases the backscattering and thus also the satellite retrievals of soil permittivity show higher values than during freezing periods.

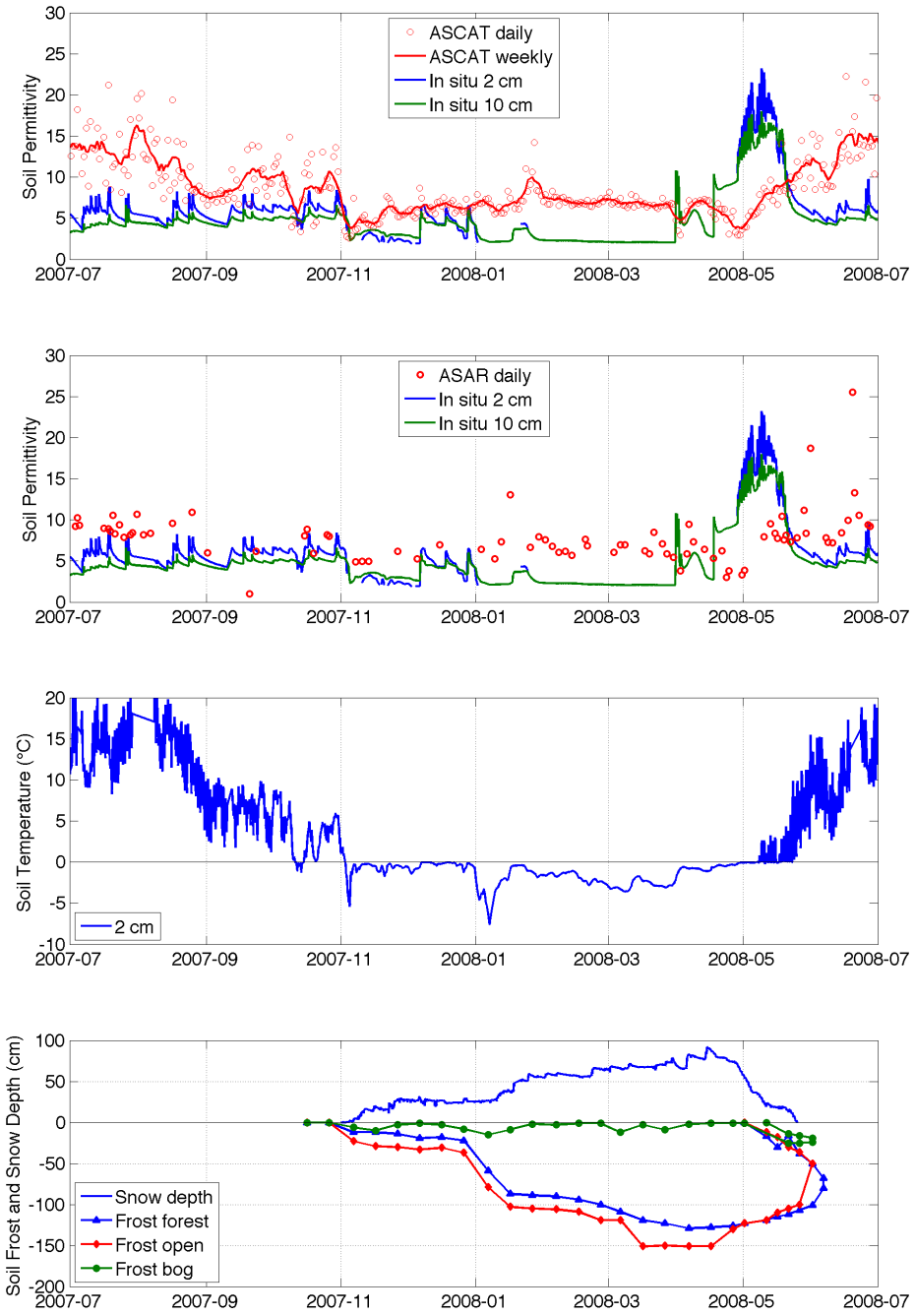

Figure 5.1: ASCAT & ASAR permittivity retrievals, and *in situ* soil permittivity, temperature, frost, and snow depth measurements for autumn 2007 and spring 2008.

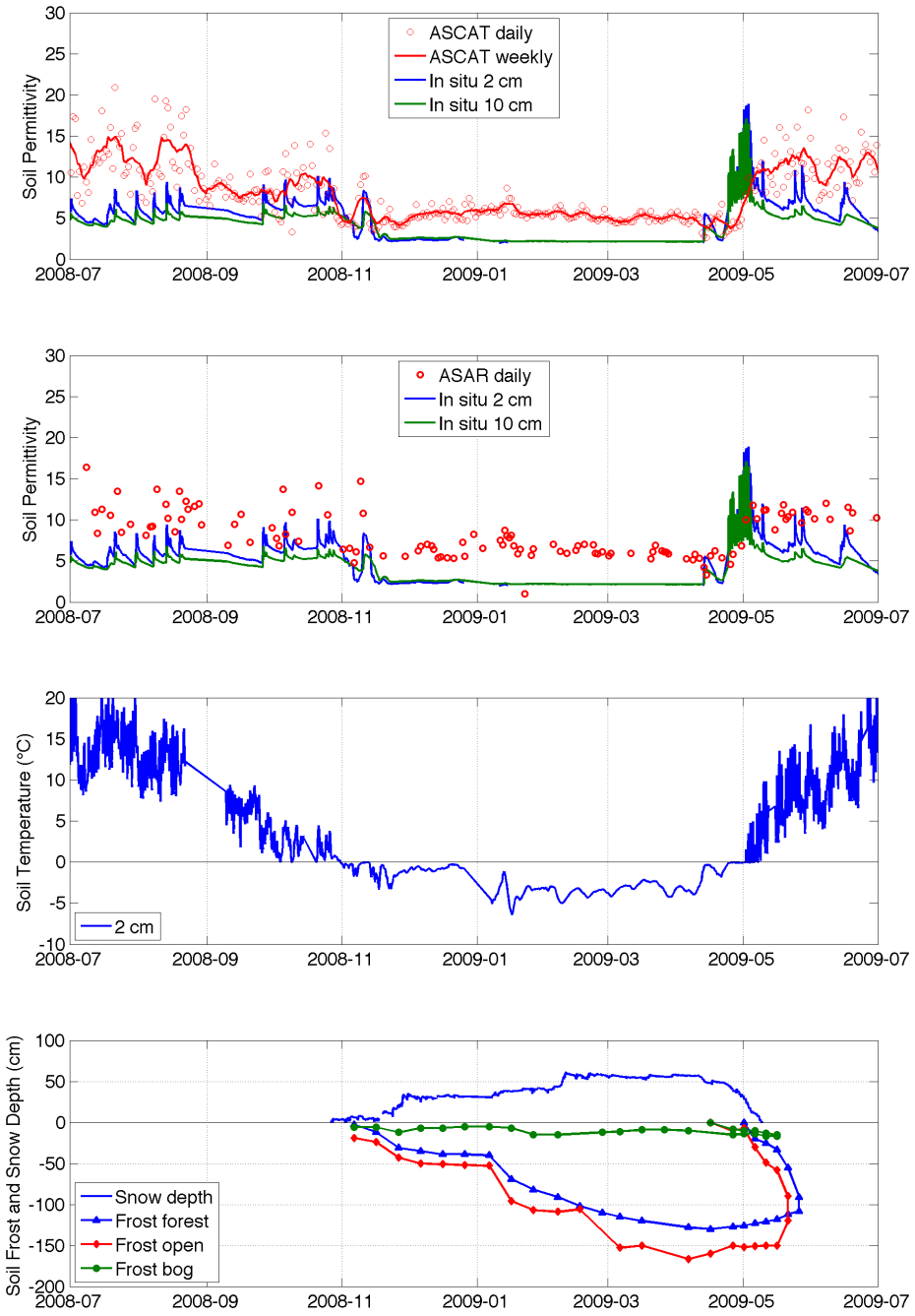

Figure 5.2: ASCAT & ASAR permittivity retrievals, and *in situ* soil permittivity, temperature, frost, and snow depth measurements for autumn 2008 and spring 2009.

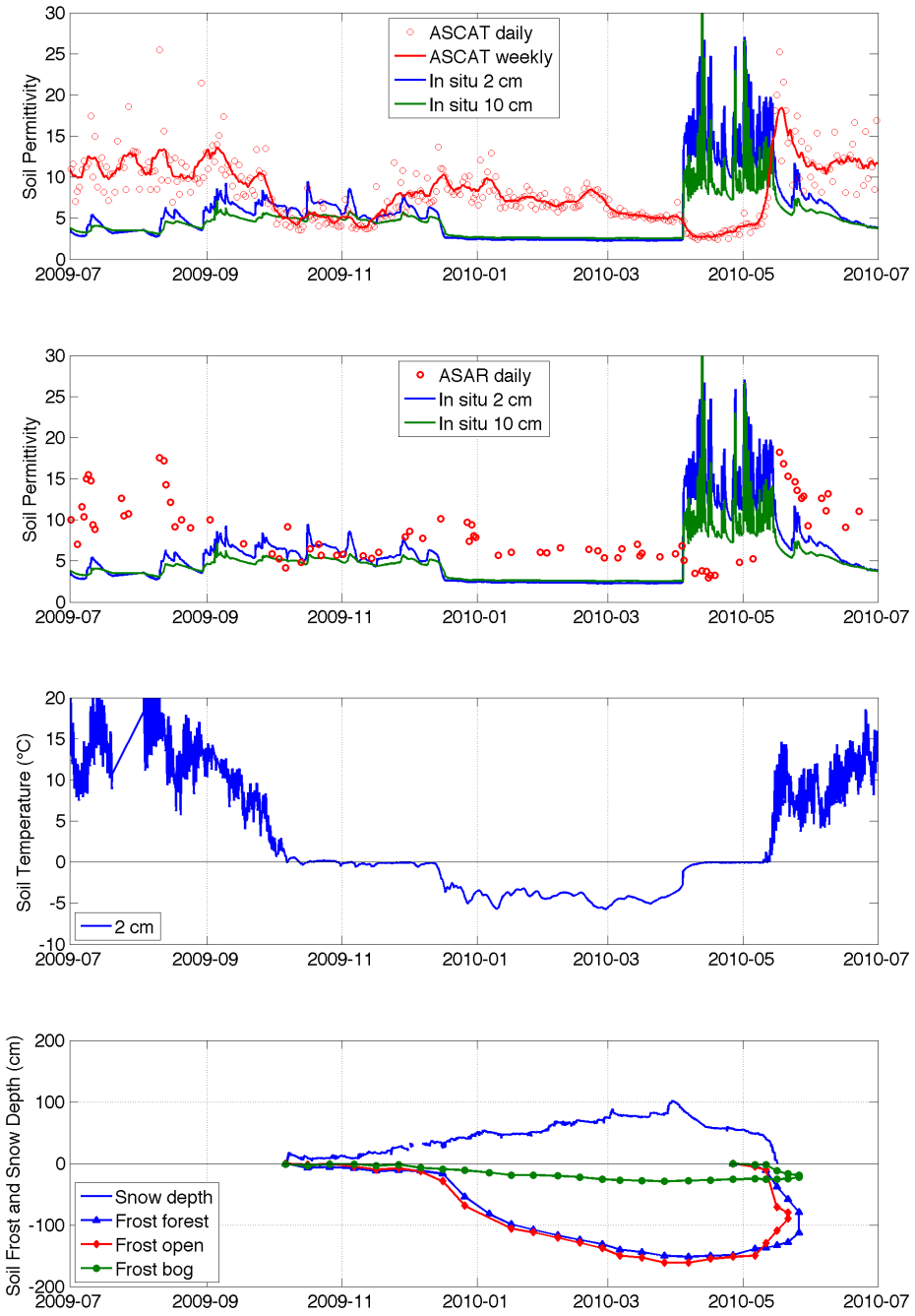

Figure 5.3: ASCAT & ASAR permittivity retrievals, and *in situ* soil permittivity, temperature, frost, and snow depth measurements for autumn 2009 and spring 2010.

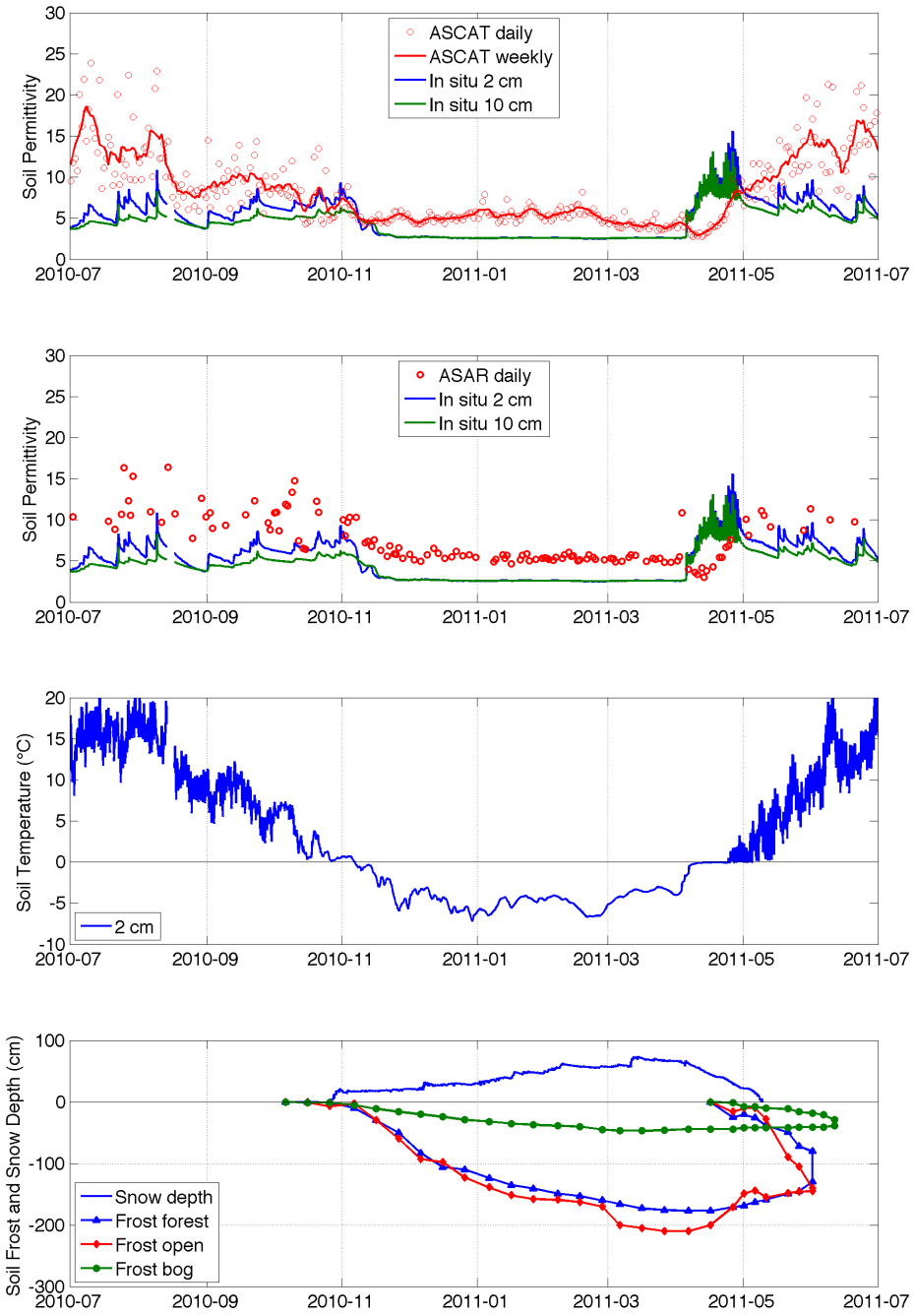

Figure 5.4: ASCAT & ASAR permittivity retrievals, and *in situ* soil permittivity, temperature, frost, and snow depth measurements for autumn 2010 and spring 2011.

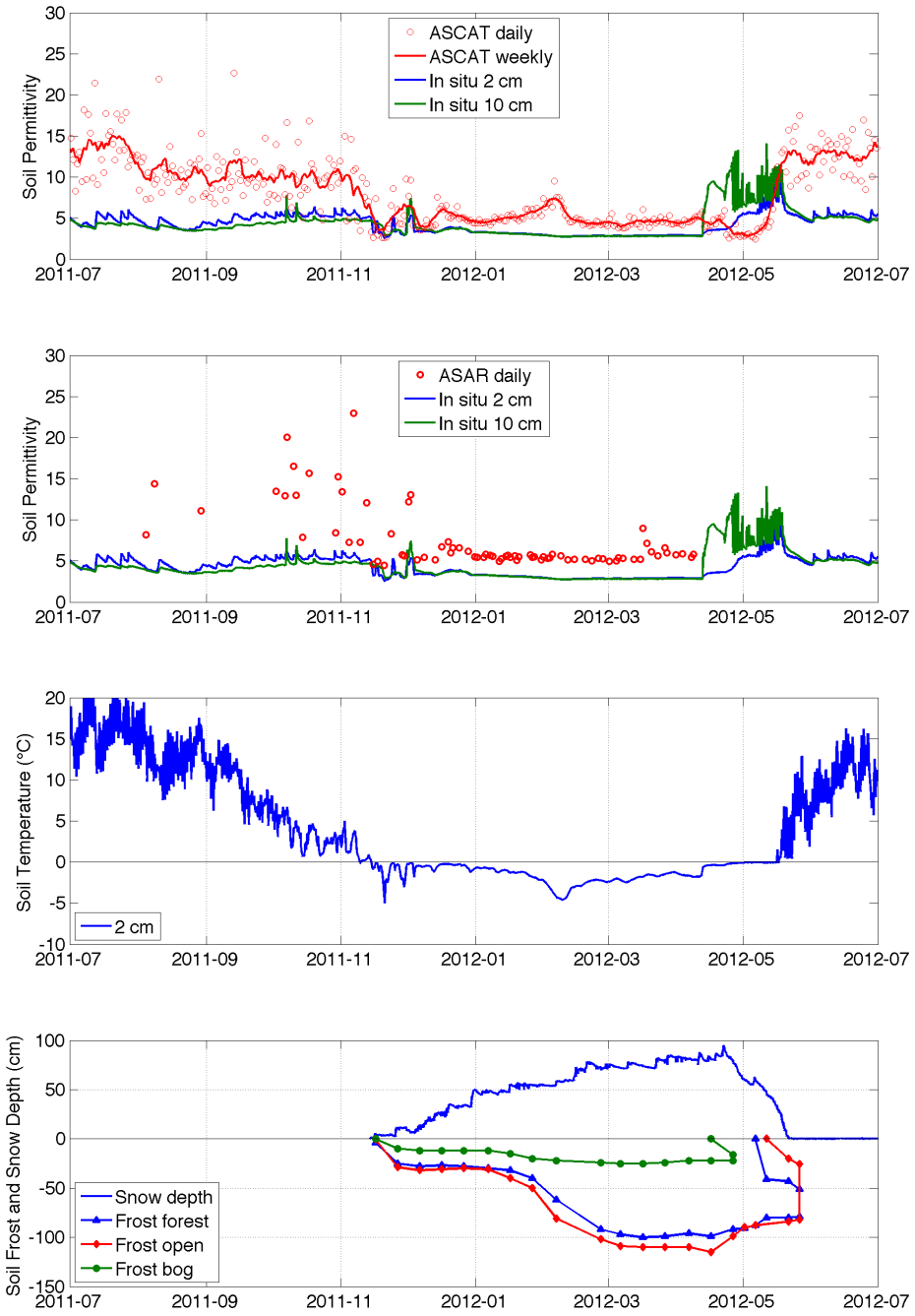

Figure 5.5: ASCAT & ASAR permittivity retrievals, and *in situ* soil permittivity, temperature, frost, and snow depth measurements for autumn 2011 and spring 2012.

5.2 Soil permittivity retrievals

Satellite based soil permittivity retrievals were compared to each other and also with *in situ* measurements. Various error estimates were calculated and scatterplots are provided for visualization.

Table 5.1 shows correlations, unbiased root mean square errors and average differences between ASCAT and ASAR soil permittivity retrievals for different years. Results are shown only for snow-free conditions. Results show moderate correlations between the retrievals during most years. Average differences show that during summers 2008 and 2009 ASCAT provides higher permittivity values (positive difference) and during 2010 ASAR provides higher permittivity values (negative difference). During 2011 there was a shortage of ASAR observations especially during summer so comparisons for ASAR are provided only for years 2008–2010. Summer 2007 has also been left out as it was only partially included in the test period.

Figure 5.6 shows scatterplots between ASCAT and ASAR soil permittivity retrievals for different years and also for the whole time period. Apart from some outliers in 2008 the plots are fairly uniform but show variation between the retrievals. ASCAT retrieval also has wider range in permittivity values than ASAR retrieval.

Table 5.1: Correlation, unbiased RMSE, average difference and the number of points between daily ASCAT and ASAR permittivity retrievals in snow-free conditions for different years.

ASCAT vs. ASAR permittivity, daily values

Year	Correlation	Unbiased RMSE	Difference	# of points
2008	0.40	4.11	0.29	57
2009	0.57	3.06	0.90	41
2010	0.66	3.24	-0.28	47
2008–2010	0.51	3.59	0.28	145

Figure 5.6: Scatterplots between daily ASCAT and ASAR permittivity retrievals in snow-free conditions for different years, line showing 1:1 relationship.

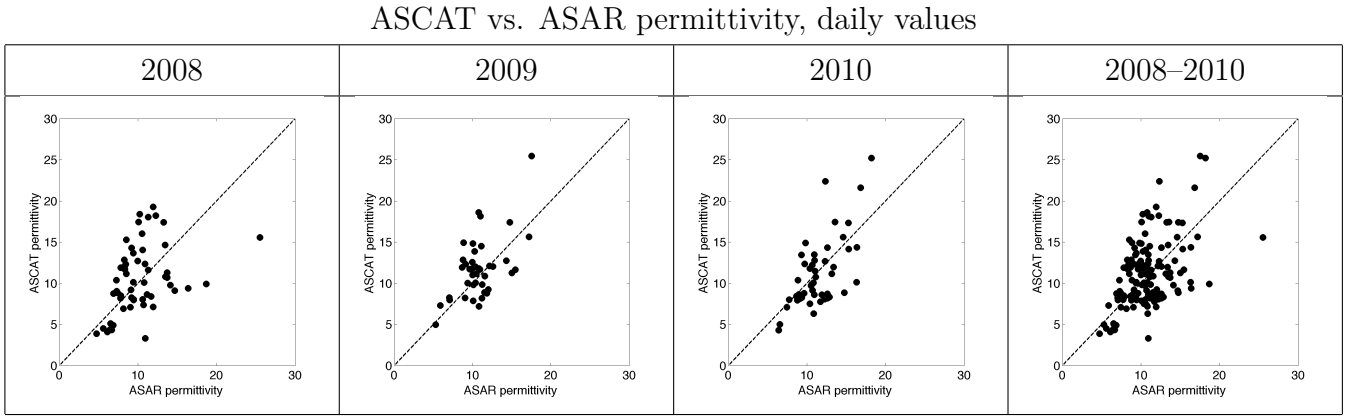

Table 5.2 shows daily ASCAT soil permittivity retrieval compared to *in situ* soil permittivity measurements at 2 centimeter and 10 centimeter depths in snow-free conditions. Correlations are fairly low and for 2009 non existent. Biases are positive and high. Comparison to measurements in 2 centimeter depth show slightly better results compared to those in 10 centimeter depth. As the penetration depth of microwaves in soil reaches 10 centimeters only at very dry conditions, this correlation is mostly an indirect effect. Figure 5.7 shows the same comparisons as scatterplots. The satellite retrieval shows higher values than *in situ* measurements, which might be caused by the difference of spatial scale as the satellite retrieval covers a larger area than the *in situ* measurement. The *in situ* measurements might also be made in drier soil than surrounding areas and not be completely representative of the whole area. Part of this difference can also result from the satellite retrieval algorithm and might be corrected with better calibration for the local conditions. The scatterplots also show less variation in *in situ* measurements made in 10 centimeter depth than in 2 centimeter depth, which is explained by only part of the moisture penetrating the soil, because of the effect of vegetation and evaporation from the surface of the soil.

Table 5.3 shows weekly ASCAT soil permittivity retrieval compared to *in situ* soil permittivity measurements at 2 centimeter and 10 centimeter depths in snow-free

Table 5.2: Correlation, unbiased RMSE, bias and the number of points between the daily ASCAT retrieval and *in situ* permittivity in snow-free conditions for different years and measurement depths.

ASCAT vs. *in situ* permittivity at 2 cm depth, daily values

Year	Correlation	Unbiased RMSE	Bias	# of points
2008	0.34	3.84	4.63	153
2009	0.02	3.38	5.33	132
2010	0.23	4.01	5.44	156
2011	0.28	3.59	6.01	191
2008–2011	0.22	3.75	5.39	632

ASCAT vs. *in situ* permittivity at 10 cm depth, daily values

Year	Correlation	Unbiased RMSE	Bias	# of points
2008	0.21	4.00	5.57	153
2009	-0.05	3.18	6.29	132
2010	0.17	4.03	6.57	156
2011	0.21	3.66	6.75	191
2008–2011	0.14	3.77	6.32	632

conditions. Results are similar to those with daily values.

If we compare ASCAT backscatter with *in situ* soil permittivity measurements, the correlation for daily values is 0.18 at 2 centimeter and 0.09 at 10 centimeter for years 2008–2011. For weekly values between ASCAT backscatter and *in situ* permittivity the correlation is 0.20 at 2 centimeter and 0.11 at 10 centimeter for years 2008–2011. These are slightly lower than between ASCAT permittivity and *in situ* permittivity, so the algorithm presented here seems to improve things a little, but not much.

Figure 5.7: Scatterplots between the daily ASCAT retrieval and *in situ* permittivity in snow-free conditions for different years and measurement depths, line showing 1:1 relationship. Axes are scaled differently, because the range of values from the satellite retrieval and *in situ* measurements are different.

ASCAT vs. *in situ* permittivity at 2 cm depth, daily values

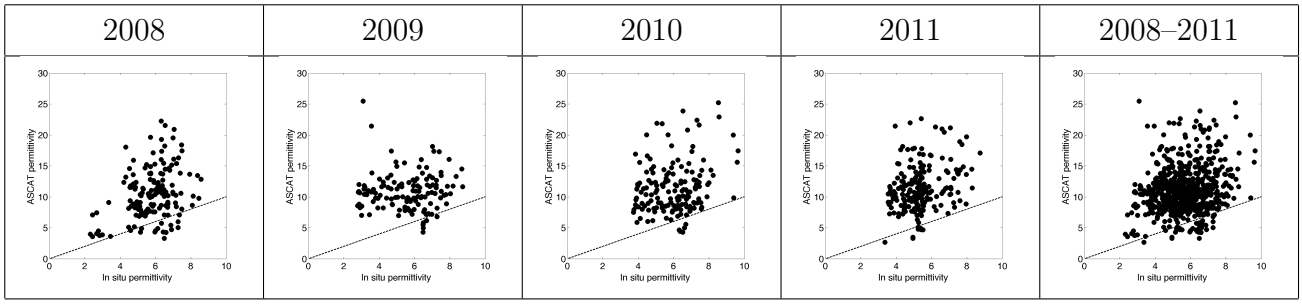

ASCAT vs. *in situ* permittivity at 10 cm depth, daily values

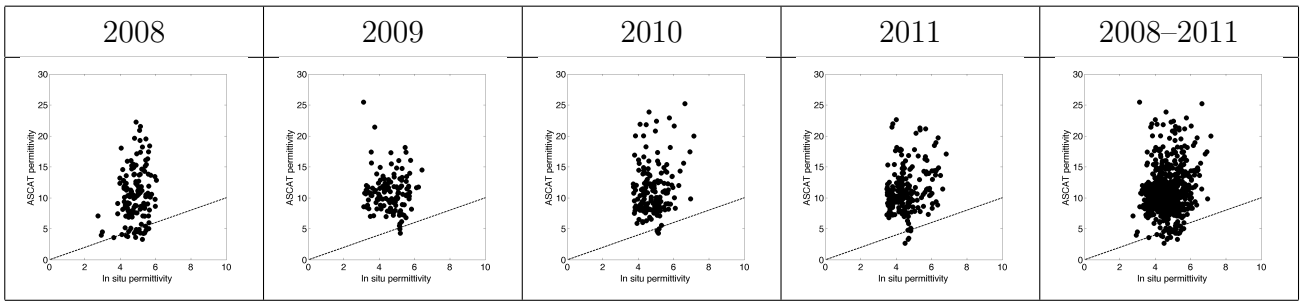

Table 5.4 shows daily and weekly ASCAT soil permittivity retrievals compared to *in situ* soil temperature in snow-free conditions. Results show some correlation between them, especially with weekly values. Figure 5.8 shows the same comparisons as scatterplots.

Correlation with temperature is quite intriguing and the reason is yet unknown. In principle, when the temperature is higher the ground should dry faster and this would yield slightly negative correlation, but the correlation observed here was positive. The backscattering model has a slight dependence on temperature but it is too small to explain this finding. The same can also be seen when comparing pure ASCAT backscatter with temperature. For years 2008–2011 the correlation

Table 5.3: Correlation, unbiased RMSE, bias and the number of points between the weekly ASCAT retrieval and *in situ* permittivity in snow-free conditions for different years and measurement depths.

ASCAT vs. *in situ* permittivity at 2 cm depth, weekly values

Year	Correlation	Unbiased RMSE	Bias	# of points
2008	0.32	2.89	4.62	153
2009	-0.03	2.19	5.32	132
2010	0.24	2.87	5.44	156
2011	0.38	2.11	6.02	191
2008–2011	0.23	2.58	5.39	632

ASCAT vs. *in situ* permittivity at 10 cm depth, weekly values

Year	Correlation	Unbiased RMSE	Bias	# of points
2008	0.15	3.01	5.56	153
2009	-0.10	1.87	6.28	132
2010	0.20	2.86	6.57	156
2011	0.31	2.16	6.76	191
2008–2011	0.16	2.56	6.32	632

is 0.48 for daily values and 0.72 for weekly values, which is very similar than the results with permittivity retrieval (0.54 and 0.71 correspondingly). When comparing *in situ* permittivity with temperature there is no correlation (-0.23 daily and -0.27 weekly for years 2008–2011, although for 2009 there is a negative correlation – -0.59 daily and -0.71 weekly – which is explained by higher temperature drying the ground and thus lowering the permittivity), as expected. Backscattering coefficient should mainly be related to permittivity and thus water content. Possible explanations could be that the satellites observe mainly vegetation and that the vegetation moisture or evaporation is related to temperature, but this observation needs further investigation.

Table 5.4: Correlation and the number of points between the daily and weekly ASCAT permittivity retrievals and *in situ* soil temperature in snow-free conditions for different years.

ASCAT permittivity vs. *in situ* temperature at 2 cm depth, daily values

Year	Correlation	# of points
2008	0.70	153
2009	0.40	132
2010	0.51	156
2011	0.47	191
2008–2011	0.54	632

ASCAT permittivity vs. *in situ* temperature at 2 cm depth, weekly values

Year	Correlation	# of points
2008	0.87	153
2009	0.56	132
2010	0.67	156
2011	0.68	191
2008–2011	0.71	632

Figure 5.8: Scatterplots between the daily ASCAT permittivity retrieval and *in situ* soil temperature in snow-free conditions for different years.

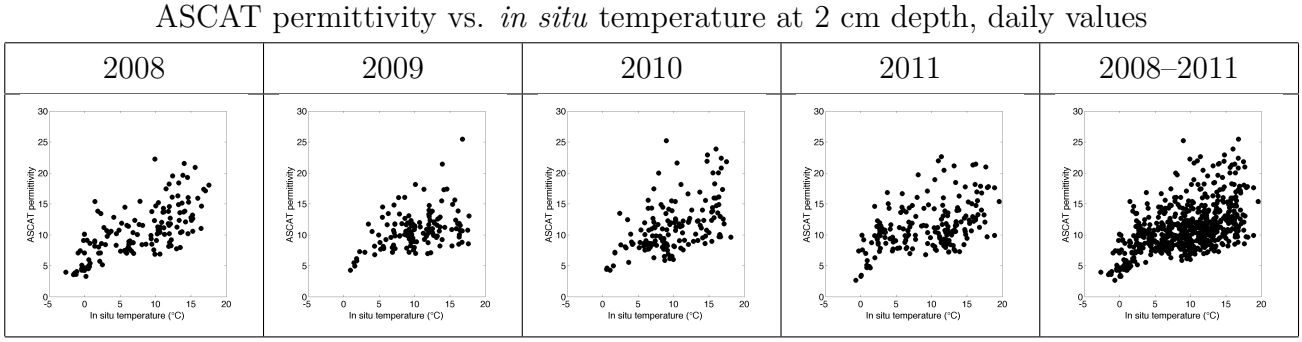

Table 5.5 shows daily ASAR soil permittivity retrieval compared to *in situ* soil permittivity measurements at 2 centimeter and 10 centimeter depths in snow-free conditions. The results do not show much correlation, similar to the results between ASCAT permittivity retrieval and *in situ* permittivity measurements. Figure 5.9 shows the same comparisons as scatterplots.

Table 5.6 shows daily ASAR soil permittivity compared to *in situ* soil temperature in snow-free conditions. Correlations are not high, but show some slight correlation during 2009. This might explain why the correlation between ASAR permittivity retrieval and *in situ* permittivity were negative for 2009 as this was the year when *in situ* permittivity and temperature had also negative correlation. Correlation between ASAR permittivity and temperature is lowest in 2010, which also has the best correlation between ASAR permittivity and *in situ* permittivity. Correlations between ASAR permittivity retrieval and temperature are lower than those between ASCAT retrieval and temperature. Figure 5.10 shows the same comparisons as scatterplots.

If we compare ASAR backscatter with *in situ* soil permittivity measurements, the correlation is 0.17 at 2 centimeter and 0.10 at 10 centimeter for years 2008–2010. These are approximately the same than between ASAR permittivity and *in situ* permittivity, so the algorithm presented here does not seem to have much effect on the results. For individual years results are more varying. In 2008 the correlation for

backscatter was 0.44 at 2 centimeters, but for permittivity retrieval it was only 0.23. At 10 centimeters the correlation was 0.30 for backscatter and 0.13 for permittivity retrieval. So here the algorithm seems to perform worse than pure backscatter. But for 2010 the situation is opposite, correlation for backscatter is 0.13 at 2 cm and 0.11 at 10 cm, when for the retrieval they are 0.43 and 0.45 respectively.

Correlation between ASAR backscatter and *in situ* temperature is 0.33 for 2008–2010 which is similar than between ASAR permittivity retrieval and temperature. For 2008 the correlation is 0.44 for backscatter and 0.33 for permittivity, so here the algorithm seems to have decreased the effect of temperature. For 2009 it is the opposite, correlation is 0.38 for backscatter and 0.49 for permittivity, so the algorithm seems to have increased the correlation with temperature.

Table 5.5: Correlation, unbiased RMSE, bias and the number of points between the daily ASAR retrieval and *in situ* permittivity in snow-free conditions for different years and measurement depths.

ASAR vs. *in situ* permittivity at 2 cm depth, daily values

Year	Correlation	Unbiased RMSE	Bias	# of points
2008	0.23	2.83	3.89	50
2009	-0.27	3.40	5.22	38
2010	0.43	2.34	4.90	46
2008–2010	0.17	2.91	4.62	134

ASAR vs. *in situ* permittivity at 10 cm depth, daily values

Year	Correlation	Unbiased RMSE	Bias	# of points
2008	0.13	2.83	4.85	50
2009	-0.40	3.09	6.23	38
2010	0.45	2.34	6.25	46
2008–2010	0.08	2.83	5.73	134

Figure 5.9: Scatterplots between the daily ASAR retrieval and *in situ* permittivity in snow-free conditions for different years and measurement depths, line showing 1:1 relationship.

ASAR vs. *in situ* permittivity at 2 cm depth, daily values

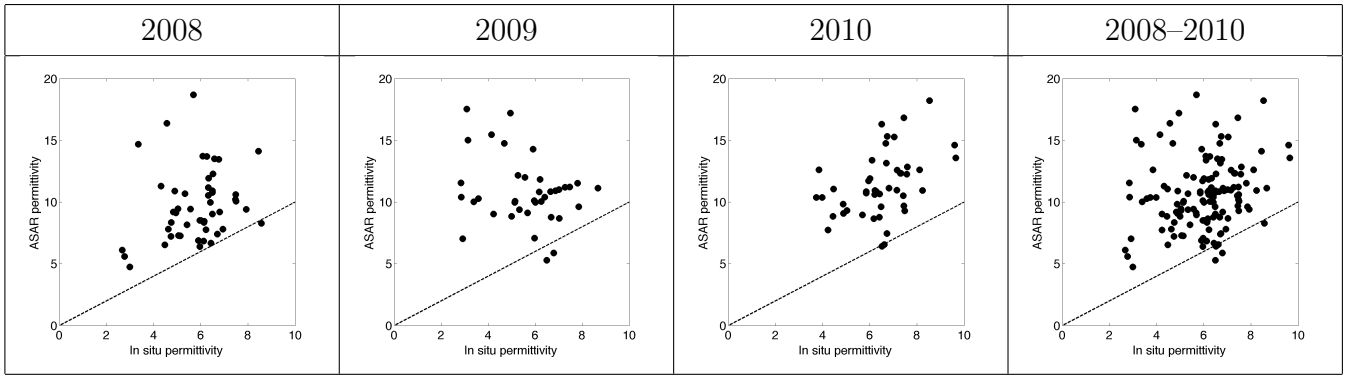

ASAR vs. *in situ* permittivity at 10 cm depth, daily values

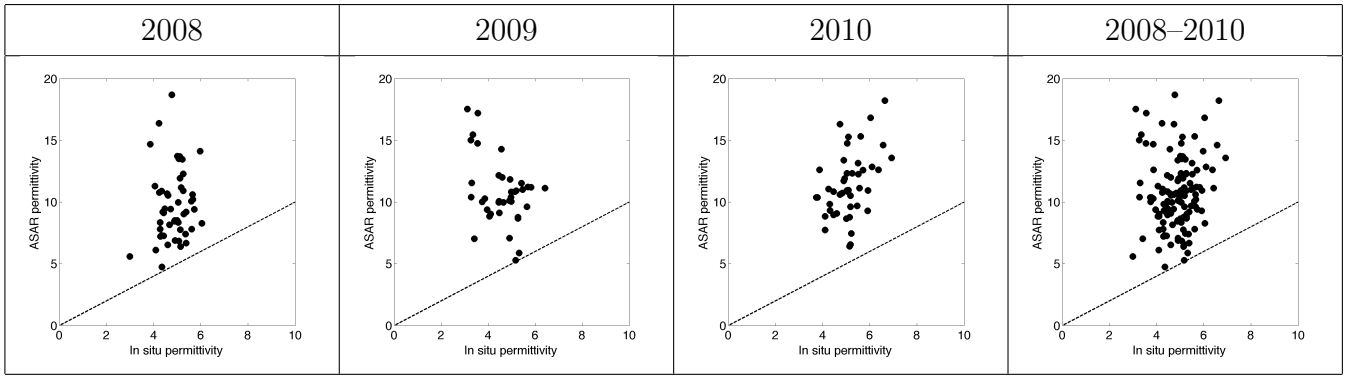

Table 5.6: Correlation and the number of points between the daily and weekly ASAR permittivity retrievals and *in situ* soil temperature in snow-free conditions for different years.

ASAR permittivity vs. *in situ* temperature at 2 cm depth, daily values

Year	Correlation	# of points
2008	0.33	50
2009	0.49	38
2010	0.21	46
2008–2010	0.35	134

Figure 5.10: Scatterplots between the daily ASAR permittivity retrieval and *in situ* soil temperature in snow-free conditions for different years.

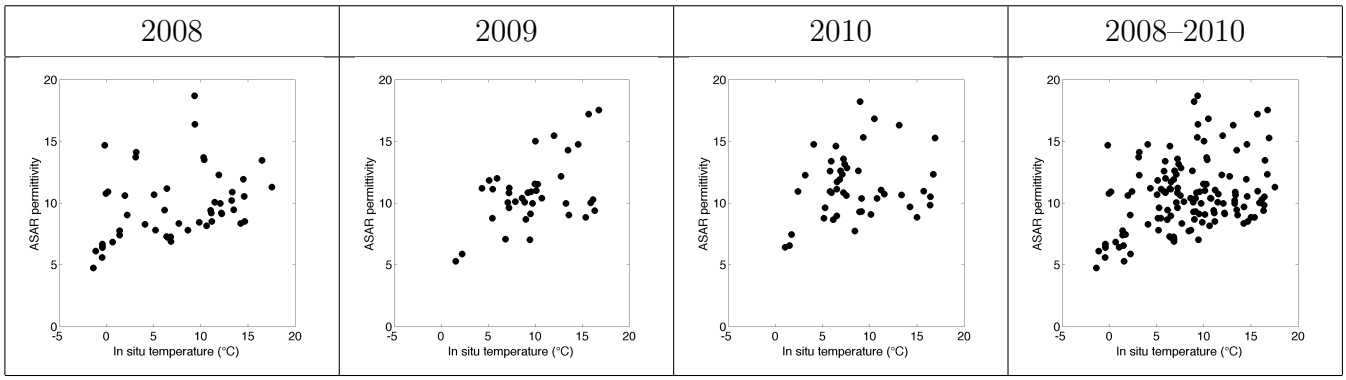

Table 5.7: Mean and standard deviation of ASCAT permittivity retrieval for different combinations of frozen and non-frozen soil and with and without snow cover for years 2007-2012 (excluding spring months from March to May).

2007–2012 (no March–May)

	Snow	No snow
Frozen	mean = 6.20	mean = 5.18
	std = 1.64	std = 2.16
	points/days = 670	points/days = 30
Non-frozen	mean = 5.74	mean = 11.13
	std = 1.82	std = 3.51
	points/days = 40	points/days = 819

5.3 Soil frost estimate

The feasibility of using satellite based soil permittivity retrievals for estimating soil freezing was studied. First the differences in backscatter values in different temperature and snow conditions were examined. Table 5.7 shows mean values, standard deviations and the number of observations for ASCAT retrieval during 2007–2012 classified by when there has been snow and no snow, and when the ground has been frozen (soil temperature $< 0°C$) and non-frozen (soil temperature $\geq 0°C$). To exclude melting snow, months March, April, and May have been filtered out. Similar values for ASAR retrieval are shown in Table 5.8.

Mean values for winter (snow and frozen ground) is much lower than mean values for summer (no snow and non-frozen ground). During autumn, if the snow has fallen before the ground has frozen (snow and non-frozen ground) the mean values are close to those from winter, being slightly lower for ASCAT and slightly higher for ASAR. Same applies when the ground has frozen before snow (no snow and frozen ground). This indicates that the satellite retrievals are affected similarly by both snow cover and soil freezing and thus detecting soil freeze might only be possible when the ground is free of snow cover, unless the snow is dry enough to not affect the satellite retrieval excessively.

Estimating soil freezing onset was studied using threshold values for soil per-

Table 5.8: Mean and standard deviation of ASAR permittivity retrieval for different combinations of frozen and non-frozen soil and with and without snow cover for years 2007-2012 (excluding spring months from March to May).

2007–2012 (no March–May)

	Snow	No snow
Frozen	mean = 6.17	mean = 7.35
	std = 1.41	std = 3.29
	points/days = 181	points/days = 9
Non-frozen	mean = 7.63	mean = 10.34
	std = 2.14	std = 3.00
	points/days = 10	points/days = 148

mittivity retrievals. Figure 5.11 shows the different estimates of soil frost onset. Estimated dates are shown for each year. Estimates for ASCAT and ASAR are based on when the permittivity retrievals are below threshold value. For ASCAT weekly values were used and for ASAR daily values. Threshold value of 5 is used for both satellite retrievals. This was approximately the mean value of ASCAT retrieval when the soil was frozen and there was no snow cover. For ASAR retrieval the mean value in these conditions was higher, but because there was not many observations and the deviation was quite high the same value as for ASCAT was decided to be used here. Soil frost dates are based on manual frost measurements in different locations. Measurements are performed three times a month (6., 16. and 26. day of each month), so the freezing can have started already on an earlier date. Because measurements are not accurate at very small values, the first date when frost has been more than 3 cm deep is shown. Onset date for daily *in situ* soil temperature at 2 cm depth falling below zero is also shown. For ASCAT and soil temperature the lines indicate the time period the values have stayed below their thresholds. Onset dates for snow depth more than 0 cm, 5 cm and 10 cm are also shown.

In 2007 ASAR has had a drop in permittivity already in September which is not shown in other measurements and thus is an error regarding frost estimation. In early October there has been a short freezing event in *in situ* soil temperature,

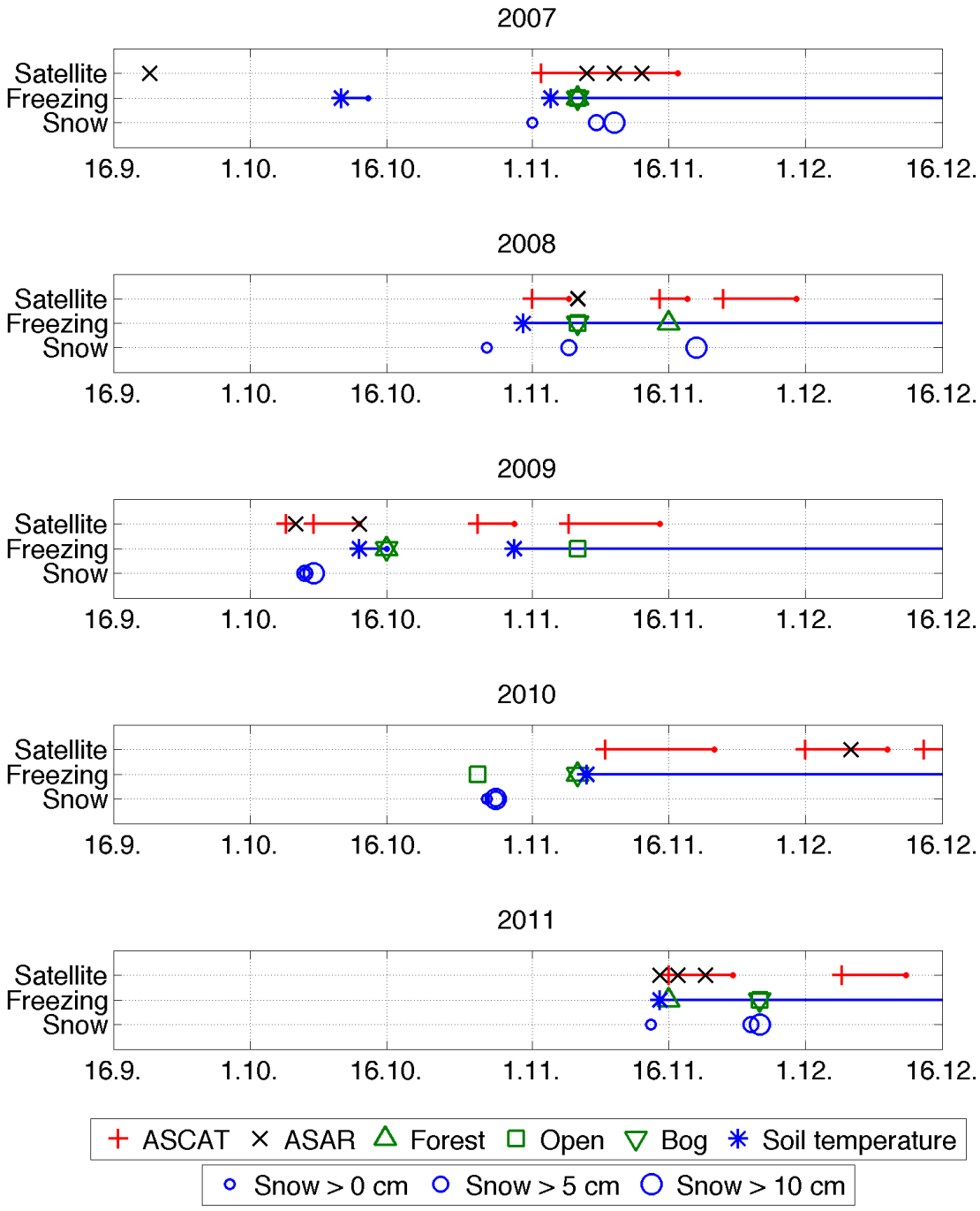

Figure 5.11: Estimates of soil freezing onset from ASCAT & ASAR retrievals compared to *in situ* frost measurements and onset of freezing from *in situ* soil temperature measurement. Lines indicate the time period the values have stayed below threshold. Onsets for snow depth more than 0 cm, 5 cm and 10 cm are also included.

but soil frost has not occurred yet and this also has not been detected by satellite retrievals. First snow has fallen at the beginning of November and shortly after that the soil temperature has dropped below zero and also the soil freezing has started at all locations. ASCAT retrieval seems to have reacted to the snowfall slightly before any soil freezing has been detected, but ASAR has responded a little bit later and coincides better with frost measurements.

In 2008 snow has fallen at the end of October but stayed quite shallow until November. Slightly later just before the November the soil temperature has dropped below zero and also ASCAT retrieval has dropped immediately at the start of November. Soil frost has been detected at the next measurement at open ground and bog locations and ASAR has indicated freezing at the same time. ASCAT retrieval has not stayed below threshold after initial drop and has two subsequent declines in the mid-November. First of these seems to coincide with soil frost detected at the forest location.

In 2009 both satellite retrievals have indicated first freezing event at the beginning of October before any snowfall or freezing at soil temperature. Snow has fallen slightly later which has resulted in another decline at ASCAT retrieval. A little bit later at the middle of October the soil temperature has dropped below zero for a short time and soil frost has been detected at forest and bog locations. ASAR has estimated another freezing event at the same time. Interestingly the soil temperature has increased to zero or above for the end of the month, even though there has been snow on the ground. ASCAT has had another decline at the end of October and third at the beginning of November. Between those the soil temperature has eventually dropped permanently below zero. Soil frost has been detected at the open ground location around the same time as the last ASCAT decline.

In 2010 soil frost has been detected at the open ground location at the end of October before any snowfall or freezing at soil temperature, which could be a measurement error. Snow has fallen shortly after that, but soil temperature and frost measurements do not detect freezing until the beginning of November. ASCAT also indicates freezing around the same time, but ASAR does not until the beginning of December.

In 2011 the first snow has fallen just before the mid-November and immediately after that the soil temperature has fallen below zero and soil frost has been detected

at the forest location. Both satellite retrievals have also indicated freezing at this time. Soil frost at open ground and bog locations has not been detected until the end of November and also snow cover has gotten thicker at the same time.

Overall ASCAT retrieval seems to agree well with the freezing estimate from in situ soil temperature for all years except 2009 which had quite exceptional weather conditions. In 2007 ASCAT seems to react to snowfall slightly before freezing, but in 2008, 2010 and 2011 the first ASCAT estimate occurs soon after the *in situ* freezing detection. Interestingly during 2008 and 2010 the ASCAT retrieval does not seem to be distracted by the snowfall occurring before any freezing has been detected in soil temperature.

ASAR retrieval seems to agree with *in situ* freezing estimates in 2007 (if we ignore the false detection already in September), 2008 and 2011. In 2007 and 2008 it reacts slightly later than ASCAT which can be caused by missing days in data or less suitable threshold value. Because of worse temporal resolution than ASCAT it is not as suitable for accurate detection of the exact moment the freezing, but can provide high spatial resolution information about differences across different locations. Likewise ASCAT, in 2009 ASAR does not seem to fare well with the peculiar conditions of that year and also in 2010 it indicates freezing too late. This could indicate that maybe there should be different threshold values for different years instead of a constant one.

After the initial freezing both satellite retrievals start to react to changes in weather and snow conditions and thus do not provide any reliable information about the frost status. Thus to use satellite retrievals for a proper soil frost product some other information about the environmental conditions like air temperature and snow cover needs to be incorporated to exclude false estimates before any freezing can have occurred and to ensure the estimate keeps the frost status during snow period.

5.4 Discussion

In [6] ESA CCI Soil Moisture product was compared to spatially weighted *in situ* measurements in Sodankylä area and found to have correlations of 0.55 (daily) and 0.84 (weekly) for 2012 and 0.62 (daily) and 0.81 (weekly) for 2013, but only 0.19 (daily) and 0.17 (weekly) for 2014. The product is based on same ASCAT obser-

vations that were used in this study, and results indicate that the performance varies heavily between different years. This could mean that the poor results observed in this work might have depended on the time period used.

Due to lack of varying measurement angles the ASCAT retrieval used constant vegetation permittivity, which may hinder the results. The ASCAT pixel used as the test area also contained some waterbodies, which cause error for the ASCAT retrieval. In ASAR retrieval they were filtered out, which was made possible by the better spatial resolution of the instrument. The observations for both instruments were a combination of different trajectories and observation times, which cause noise to the retrieval and also may produce error when comparing to daily averages of *in situ* measurements. ASAR retrieval also combined two different polarizations and even though the backscattering model compensates this, it can cause some variability to the results. To compensate the errors the differences in trajectories and polarization cause, a more unified dataset could be used, but that would also greatly limit the temporal resolution of the retrieval. Overpasses from mornings and evenings could be investigated separately, or use *in situ* measurements only close to the time of satellite observation. In latter case it could still be a little bit problematic to determine which time period to use for the *in situ* measurements, as the satellite retrievals react faster to changes in moisture/permittivity especially in vegetation than the moisture/permittivity measured from soil does. The backscattering model used for the satellite retrievals was calibrated for a different location so calibrating it specifically for the test area might improve the results. Possible inaccuracies in the forest stem volume data used in ASAR retrieval can also affect the results for the satellite estimate.

As the *in situ* measurements used in this study were only from one place, it is possible that it is not representative of the whole satellite retrieval pixel. This can be compensated using several measurements from different soil and terrain types and calculating a weighted average for the satellite footprint, as was done in [6]. ASAR retrieval could also be produced for a smaller area than was used in this study.

One big question regarding satellite retrievals of soil variables is that do they really manage to observe soil in heavily vegetated areas like Sodankylä, or are they only reacting to changes in vegetation. And if they manage to observe soil, how deep can they measure. In this study the results were better when compared to

in situ measurements made from 2 cm depth than from 10 cm depth, which indicates that the satellites measure only the very top layer of the soil. This is consistent with [23], which indicated that microwaves penetrate to 10 cm depth only at very dry conditions. Using a lower frequency instrument than the ones used in this work could decrease the effect of vegetation and help observing the soil beneath it and also enable observations deeper into the soil.

The question about penetration depth applies also to frost detection. The satellites are only seeing the very top layer of the soil at the most, so they can only detect when the surface of the ground freezes. Comparing backscatter values of frozen and snow covered grounds indicated that the satellites might not be able to distinguish frozen and non-frozen grounds when there is snow present. Still the comparison of freezing onsets showed that the satellite estimates agreed with soil temperature during most of the years, independent of the snow cover. Dry snow has less effect on backscattering than wet snow, so the effect of snow is dependent on temperature.

The method for detecting soil freezing showed promising results, but determining the permittivity threshold needs further studies to find best values for each instrument and to investigate if there is variability between different years and locations. In [15] ASCAT backscatter is used to determine freeze/thaw conditions and is found to compare well against modeled soil temperature data and air temperature measurements across the northern hemisphere. ASCAT retrieval is also compared with *in situ* soil temperature measurements at four different sites. The method is based on a threshold-analysis and incorporates decision trees and anomaly detection modules. These results indicate that active microwave instruments can potentially be used for remote sensing of soil freezing.

Chapter 6

Summary and conclusions

In this work, the remote sensing of soil permittivity and soil freezing using satellite microwave radars over boreal forested area was investigated. Comparisons to *in situ* measurements were conducted in Sodankylä in Northern Finland. Remote sensing was done using two different satellite radars, ASCAT and ASAR. ASCAT is a scatterometer and has a good temporal resolution, but coarse spatial resolution. ASAR is a synthetic aperture radar (SAR) and has better spatial resolution, but worse temporal resolution. A semi-empirical forest backscattering model was applied to datasets from both instruments to retrieve soil permittivity values.

Results show that the permittivity values from ASCAT and ASAR correlate with each other, but not very well with *in situ* permittivity measurements. ASCAT retrieval has some correlation with *in situ* temperature measurements, which might have an impairing effect on correlation with *in situ* permittivity. The reason for this connection with temperature is unknown and needs further research. ASAR retrieval does not seem to be affected by the temperature as much as the ASCAT one.

During autumn periods the satellite permittivity retrievals seem to be similarly affected by both snow cover and soil freezing. This indicates that the retrievals can be used for soil frost detection but only when there is no snow cover. Still, when comparing the onset dates of soil freezing estimates from satellite retrievals to those from *in situ* soil temperature and soil frost measurements they coincide quite well for most of the years regardless of the moment of the first snowfall. Further studies for a more refined way to determine the permittivity threshold value for frozen soil

could improve these results, and for producing a proper soil freeze product some auxiliary information about air temperature and snow cover might be needed to filter out false estimates and the effect of snow cover on the retrieval.

Bibliography

[1] J. B. Campbell. *Introduction to Remote Sensing, Third Edition.* The Guilford Press, 2002.

[2] T. M. Lillesand and R. W. Kiefer. *Remote Sensing and Image Interpretation, Third Edition.* John Wiley & Sons, 1994.

[3] M. C. Dobson, F. T. Ulaby, M. T. Hallikainen, and M. A. El-Rayes. Microwave Dielectric Behavior of Wet Soil – Part II: Dielectric Mixing Models *IEEE Transactions on Geoscience and Remote Sensing*, vol. GE-23, no. 1, 1985.

[4] G. C. Topp, J. L. Davis, and A. P. Annan. Electromagnetic determination of soil water content: measurement in coaxial transmission lines. *Water Resources Research*, vol. 16, p. 574–582, 1980.

[5] S. Bircher, M. Andreasen, J. Vuollet, J. Vehviläinen, K. Rautiainen, F. Jonard, L. Weihermüller, E. Zakharova, J.-P. Wigneron, and Y. H. Kerr. Soil moisture sensor calibration for organic soil surface layers, *Geoscientific Instrumentation, Methods and Data Systems*, vol. 5, p. 109–125, 2016.

[6] J. Ikonen, J. Vehviläinen, K. Rautiainen, T. Smolander, J. Lemmetyinen, S. Bircher, and J. Pulliainen. The Sodankylä in-situ soil moisture observation network: An example application to ESA CCI soil moisture product evaluation. *Geoscientific Instrumentation, Methods and Data Systems*, vol. 5, p. 95–108, 2016.

[7] J. T. Pulliainen, T. Manninen, and M. T. Hallikainen. Application of ERS-1 Wind Scatterometer Data to Soil Frost and Soil Moisture Monitoring in Boreal Forest Zone. *IEEE Transactions on Geoscience and Remote Sensing*, vol. 36, no. 3, 1998.

[8] International Soil Moisture Network. (2017, November 27). Retrieved from http://www.esa.int/Our_Activities/Observing_the_Earth/SMOS

[9] SMAP – Soil Moisture Active Passive. (2017, November 27). Retrieved from http://smap.jpl.nasa.gov/

[10] International Soil Moisture Network. (2017, November 27). Retrieved from https://ismn.geo.tuwien.ac.at

[11] ESA CCI Soil Moisture. (2017, November 27). Retrieved from http://www.esa-soilmoisture-cci.org/

[12] T. Zhang, R. L. Armstrong. Soil freeze/thaw cycles over snow-free land detected by passive microwave remote sensing *Geophysical Research Letters*, vol. 28, issue 5, 2001.

[13] K. Rautiainen, T. Parkkinen, J. Lemmetyinen, M. Schwank, A. Wiesmann, J. Ikonen, C. Derksen, S. Davydov, A. Davydova, J. Boike, M. Langer, M. Drusch, and J. Pulliainen. SMOS prototype algorithm for detecting autumn soil freezing. *Remote Sensing of Environment*, vol. 180, p. 346–360, 2016.

[14] T. Jagdhuber, J. Stockamp, I. Hajnsek, and R. Ludwig. Identification of Soil Freezing and Thawing States Using SAR Polarimetry at C-Band *Remote Sensing*, vol. 6, no. 3, 2014.

[15] V. Naeimi, C. Paulik, A. Bartsch, W. Wagner, R. Kidd, S.-E. Park, K. Elger, and J. Boike. ASCAT Surface State Flag (SSF): Extracting Information on Surface Freeze/Thaw Conditions From Backscatter Data Using an Empirical Threshold-Analysis Algorithm. *IEEE Transactions on Geoscience and Remote Sensing*, vol. 50, no. 7, 2012.

[16] C. J. Tuckera, J. E. Pinzona, M. E. Browna, D. A. Slaybacka, E. W. Paka, R. Mahoneya, E. F. Vermotea, and N. El Saleousa. An extended AVHRR 8-km NDVI dataset compatible with MODIS and SPOT vegetation NDVI data. *International Journal of Remote Sensing*, vol. 26, issue 20, 2005.

[17] G. Zheng and L. Monika Moskal. Retrieving Leaf Area Index (LAI) Using Remote Sensing: Theories, Methods and Sensors. *Sensors*, vol. 9, no. 4, 2009.

[18] M. Vreugdenhil, W. A. Dorigo, W. Wagner, R. A. M. de Jeu, S. Hahn, and M. J. E. van Marle. Analyzing the Vegetation Parameterization in the TU-Wien ASCAT Soil Moisture Retrieval. *IEEE Transactions on Geoscience and Remote Sensing*, vol. 54, no. 6, 2016.

[19] D. J. Griffiths. *Introduction to Electrodynamics, Third Edition.* Prentice-Hall, 1999.

[20] J. D. Jackson. *Classical Electrodynamics, Third Edition.* John Wiley & Sons, 1999.

[21] J. Tyynelä. *Polarization Studies in Electromagnetic Scattering by Small Solar-System Particles.* Ph.D. Dissertation, Report Series in Astonomy 4, 2011.

[22] P. Lorrain and D. R. Corson. *Electromagnetism, Principles and Applications, Second Edition.* W. H. Freeman and Company, 1997.

[23] F. T. Ulaby, R. K. Moore, and A. K. Fung. *Microwave remote sensing: Active and Passive, Volume II: Radar Remote Sensing and Surface Scattering and Emission Theory.* Addison-Wesley Publishing Company, 1982.

[24] C. F. Bohren and D. R. Huffman. *Absorption and Scattering of Light by Small Particles.* John Wiley & Sons, 1983.

[25] A. Räisänen and A. Lehto. *Radiotekniikka.* Otatieto, 1999.

[26] K. Luojus. *Remote Sensing of Snow-Cover for the Boreal Forest Zone Using Microwave Radar.* Ph.D. Dissertation, Finnish Meteorological Institute Contributions 77, 2009.

[27] K. S. Chen, T.-D. Wu, L. Tsang, Q. Li, J. Shi, and A. K. Fung. Emission of Rough Surfaces Calculated by the Integral Equation Method With Comparison to Three-Dimensional Moment Method Simulations. *IEEE Transactions on Geoscience and Remote Sensing*, vol. 41, no. 1, 2003.

[28] J. Pulliainen. *Kaukokartoitushavaintojen mallinnus- ja tulkintamenetelmät. Opetusmonisteet 2002 ja 2003.* TKK, avaruustekniikan laboratorio.

[29] F. T. Ulaby, K. McDonald, K. Sarabandi, and M. C. Dobson. Michigan Microwave Canopy Scattering Models (MIMICS). *Proceedings of IGARSS '88 Symposium*, vol. 2, 1988.

[30] Y. Oh, K. Sarabandi, and F. T. Ulaby. An Empirical Model and an Inversion Technique for Radar Scattering from Bare Soil Surfaces *IEEE Transactions on Geoscience and Remote Sensing*, vol. 30, no. 2, 1992.

[31] P. Dubois, J. van Zyl, and T. Engman. Measuring soil moisture with imaging radars. *IEEE Transactions on Geoscience and Remote Sensing*, vol. 33, no. 4, 1995.

[32] H. Ewe, H. Chuah, and A. Fung. A backscatter model for a dense discrete medium: Analysis and numerical results. *Remote Sensing of Environment*, vol. 65, 1998.

[33] Metop is a series of three polar orbiting meteorological satellites which form the space segment component of the overall EUMETSAT Polar System (EPS). (2017, December 12). Retrieved from https://www.eumetsat.int/website/home/Satellites/CurrentSatellites/Metop/index.html

[34] ASCAT Product Guide. (2017, December 12). Retrieved from http://www.eumetsat.int/website/wcm/idc/idcplg?IdcService=GET_FILE&dDocName=PDF_ASCAT_PRODUCT_GUIDE&RevisionSelectionMethod=LatestReleased&Rendition=Web

[35] Envisat – Mission Overview. (2017, December 12). Retrieved from http://www.esa.int/Our_Activities/Observing_the_Earth/Envisat/Mission_overview

[36] Multi-source National Forest Inventory. (2017, December 1). Retrieved from http://www.metla.fi/ohjelma/vmi/vmi-moni-en.htm

[37] Avoimet ympäristötietojärjestelmät. (2018, March 21). Retrieved from http://www.syke.fi/fi-FI/Avoin_tieto/Ymparistotietojarjestelmat

[38] J. Pulliainen, M. Engdahl, and M. Hallikainen. Feasibility of multi-temporal interferometric SAR data for stand-level estimation of boreal forest stem volume *Remote Sensing of Environment*, 85 (2003): 397–409, 2003.

[39] R. J. Barlow. *Statistics. A Guide to the Use of Statistical Methods in the Physics Sciences.* John Wiley & Sons, 1989.

[40] J. T. Koskinen, J. T. Pulliainen, K. P. Luojus, and M. Takala. Monitoring of Snow Cover Properties During the Spring Melting Period in Forested Areas. *IEEE Transactions on Geoscience and Remote Sensing*, vol. 48, no. 1, 2010.

[41] M. T. Hallikainen, F. T. Ulaby, M. C. Dobson, M. A. El-Rayes, and L.-K. Wu. Microwave Dielectric Behavior of Wet Soil – Part I: Empirical Models and Experimental Observations. *IEEE Transactions on Geoscience and Remote Sensing*, vol. GE-23, no. 1, 1985.

[42] A. Griesfeller, W. A. Lahoz, R. A. M. de Jeu, W. Dorigo, L. E. Haugen, T. M. Svendby, and W. Wagner. Evaluation of satellite soil moisture products over Norway using ground-based observations. *International Journal of Applied Earth Observation and Geoinformation*, vol. 45, p. 155–164, 2016.

[43] M. Holopainen and P. Pulkkinen. *Tilastolliset menetelmät* Werner Söderström, 2002.